UC San Diego
UC San Diego Electronic Theses and Dissertations

Title

Diode laser measurement of H_2O, CO_2, and temperature in gas turbine exhaust through the application of wavelength modulation spectroscopy

Permalink

https://escholarship.org/uc/item/77j1c6nr

Author

Leon, Marco E.

Publication Date

2007

Peer reviewed|Thesis/dissertation

UNIVERSITY OF CALIFORNIA, SAN DIEGO

Diode Laser Measurement of H_2O, CO_2, and Temperature in Gas Turbine Exhaust

through the Application of Wavelength Modulation Spectroscopy

A thesis submitted in partial satisfaction of the

requirements for the degree Master of Science

in

Engineering Sciences (Mechanical Engineering)

by

Marco E. Leon

Committee in charge:

Professor Steven G. Buckley, Chair
Professor Robert J. Cattolica
Professor George R. Tynan

2007

The thesis of Marco E. Leon is approved:

_____

_____

_____
                                                              Chair

University of California, San Diego

2007

DEDICATION

To my parents, Ralph Leon and Iren Schio, for always supporting my education.

TABLE OF CONTENTS

LIST OF FIGURES

LIST OF TABLES

ACKNOWLEDGEMENTS

ABSTRACT OF THE THESIS

Diode Laser Measurement of H_2O, CO_2, and Temperature in Gas Turbine Exhaust

through the Application of Wavelength Modulation Spectroscopy

by

Marco E. Leon

Master of Science in Engineering Sciences (Mechanical Engineering)

University of California, San Diego, 2007

Professor Steven G. Buckley, Chair

Tunable Diode Laser Absorption Spectroscopy (TDLAS) provides an accurate, fast, and non-intrusive solution for species and temperature measurement. The application of this technology to measure temperature, H_2O, and CO_2 content from an industrial gas turbine has been demonstrated by this research. The multi-gas sensor system, consisting of inexpensive commercially available tunable diode lasers used in the telecommunications industry, uses Wavelength Modulation Spectroscopy (WMS) to quantify path-averaged temperature and concentrations. H_2O and CO_2 spectroscopic information was first gathered in the laboratory and then the system was packaged for field use. The work culminated in an eight-day test in April 2006 where actual stationary gas turbine emissions data were captured. The results demonstrate the capability for measurement of temperature, H_2O, and CO_2 in an industrial environment using two tunable diode lasers.

CHAPTER 1: Introduction

Tunable Diode Laser Absorption Spectroscopy (TDLAS) provides an accurate, fast, and non-intrusive solution for species and temperature measurement. The application of this technology to measure temperature, H_2O, and CO_2 content from an industrial gas turbine has been demonstrated by this research. The multi-gas sensor system, consisting of inexpensive commercially available tunable diode lasers used in the telecommunications industry, uses Wavelength Modulation Spectroscopy (WMS) to quantify path-averaged temperature and concentration. H_2O and CO_2 spectroscopic information was first gathered in the laboratory and then the system was packaged for field use. The work culminated in an eight-day test in April 2006 where actual stationary gas turbine emissions data was measured.

Near-infrared tunable diode lasers have been used over the past two decades by laboratory researchers to measure many combustion-relevant species. The Beer-Lambert Law forms the theoretical framework for this work by relating the absorption of laser light by a molecule to its concentration. The development of WMS over the past decade has greatly increased the sensitivity of TDLAS. Research by Mohammadreza Gharavi and advisor Steven Buckley at UCSD laid the foundation for the field test data presented in this thesis by successfully using WMS to measure H_2O and CH_4. The capability to measure CO_2 in a portable multiplexed system with H_2O makes this work novel.

The field-testing was performed on one of the gas turbines at the UCSD utility plant. A Fourier Transform Infrared (FTIR) system was also employed to gather data

along with the TDLAS system. In this thesis, both sets of data are compared against the gas turbine operating data.

TDLAS is promising for commercial use, because it is fast, non-intrusive, and accurate. It has the potential to be inexpensive and would be less maintenance-intensive compared to current Combustion Emissions Monitoring Systems (CEMS) that require calibration gases and frequent inspection. With data quantification capabilities on the millisecond time scale, TDLAS could also be used for active control of commercial power systems, like gas turbines.

The next chapter provides an overview of TDLAS fundamentals and WMS theory along with the historical background of these technologies. Chapter 3 covers the experimental setup used in the laboratory and field. The conversion of TDLAS data to temperature and concentration is presented in Chapter 4. Chapter 5 provides the field experimental data collected from the TDLAS, FTIR, and gas turbine systems. The final chapter summarizes the findings and outlines potential future work.

CHAPTER 2: Wavelength Modulation Spectroscopy

2.1 Introduction

Distributed Feedback (DFB) lasers and infrared detectors have been widely used by the telecommunications industry, resulting in increased availability and low cost. Fiber-pigtailed tunable diode lasers, which fall in this category, are especially attractive for combustion diagnostics because of their small size and ability to be mounted away from harsh environments. Since the measurements are based on optical absorption, process intrusion is not an issue. An overview of the fundamentals, development, and techniques of TDLAS and WMS will be covered in this chapter.

2.2 Fundamentals of TDLAS

To understand TDLAS, it is necessary to begin with the physical phenomena of the absorption of electromagnetic waves by gas-phase molecules. Molecules only absorb or emit light at certain characteristic wavelengths; a scan across wavelength space showing absorption or emission lines is commonly referred to as the spectrum of the molecule. The spectrum can be measured in the laboratory and/or calculated using quantum mechanics. At infrared wavelengths, the spectrum is the result of particular rotational-vibrational effects of the atoms in the molecule. Observed spectroscopic transitions of molecules are results of the quantization of energy. A molecule may possess rotational energy (bodily rotation about its center of gravity), vibrational energy (periodic displacement of its atoms from their equilibrium positions), and electronic energy (continuous electron movement).

The key equation of absorption spectroscopy is the Beer-Lambert Law, which relates the transmission of light to molecular species absorption:

$$I(v) = I_0(v)e^{-k_v L},$$ (2.1)

Here $I(v)$ is the intensity of the laser light after it has passed through the region of interest (attenuated laser light intensity), $I_0(v)$ is the initial intensity of the laser light (unattenuated laser light intensity), k_v is the absorption coefficient (cm^{-1}), and L is the path length (cm) the light traverses through the region of interest. The amount of laser light at frequency v that is absorbed is the product $k_v L$. The absorbance, $\alpha(v)$, can be calculated from:

$$\alpha(v) \equiv -\ln\left(\frac{I(v)}{I_o(v)}\right) = k_v L = p_{abs} S(T)\phi(v - v_0)L,$$ (2.2)

where p_{abs} is the partial pressure (torr) of the of the absorbing molecule, $S(T)$ is the absorption line strength ($cm^{-2}torr^{-1}$) which is solely a function of temperature, T, and $\phi(v - v_0)$ is the line shape function ($1/cm^{-1}$).

The line shape function is dependent on temperature by Doppler broadening effects and the partial pressure of all quenching gases in the laser region through collisional broadening effects. When the Doppler effect is dominant, the line shape function is normally represented by a Gaussian. In instances where only collisional effects are important, the line shape function is represented by a Lorentzian. However, in most combustion applications both Doppler and pressure broadening effects play a role and therefore a Voigt function is typically used to represent the line shape.

2.3 Development of TDLAS

In the late 1960's, direct current injection semiconductor lasers were used to measure species concentrations. By 1974, tunable mid-infrared diode lasers were used to measure CO from automobile traffic (Ku, Hinkley, and Sample 1975). Widespread use did not occur since the lasers had low output power (tens of μW), multimode operation, and required cryogenic cooling. The development of near-infrared room temperature single mode diode lasers packaged with on-board thermoelectric cooling opened the door for widespread species measurements.

Tunable diode lasers may be used for spectroscopy as the laser optical frequency is tuned across a selected absorption transition of a particular species. The frequency can be tuned by changing the laser temperature or by changing the drive current. Several techniques exist for laser modulation and signal interpretation. In all cases, the laser frequency is kept near the center of the molecular transition of interest by adjusting the laser temperature. The frequency of the laser light is then tuned using injection current. The type of current modulation defines the different methods of absorption spectroscopy.

The most common method of injection current modulation is direct absorption, which uses a slow ramp modulation of the current over an entire absorption line. Species concentration is calculated by total integration of the measured absorption line. A typical experimental setup is shown in Figure 2.1.
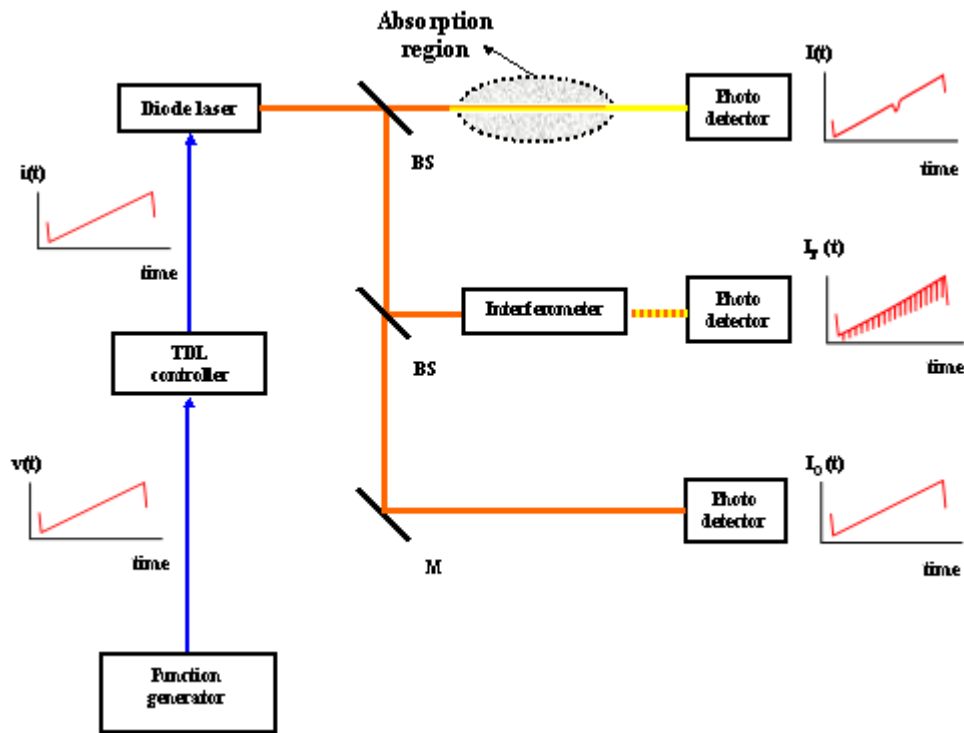
Figure 2.1: Typical experimental setup for direct absorption spectroscopy (from M. Gharavi)

There are several key drawbacks to the direct absorption technique. The primary

disadvantage is the low sensitivity associated with direct absorption. In direct absorption

the measurement is often a small change in a large signal (the laser), leading to relatively

low sensitivity. In this mode, the signal can be very sensitive to fluctuating backgrounds

common with high temperature measurements. Second, integration over the whole

spectrum is not always possible due to interference between transitions or spectral

broadening. And finally, the technique is heavily dependent on the measured reference

signal.

The technique used for this research is Wavelength Modulation Spectroscopy

(WMS). In WMS, the laser injection current is swept over a transition of interest (as in

direct absorption) at a frequency of 50 to 200 Hz with the addition of a small sinusoidal

modulation of 10 to 50 kHz superimposed on the signal. A typical experimental setup is

shown in Figure 2.2.
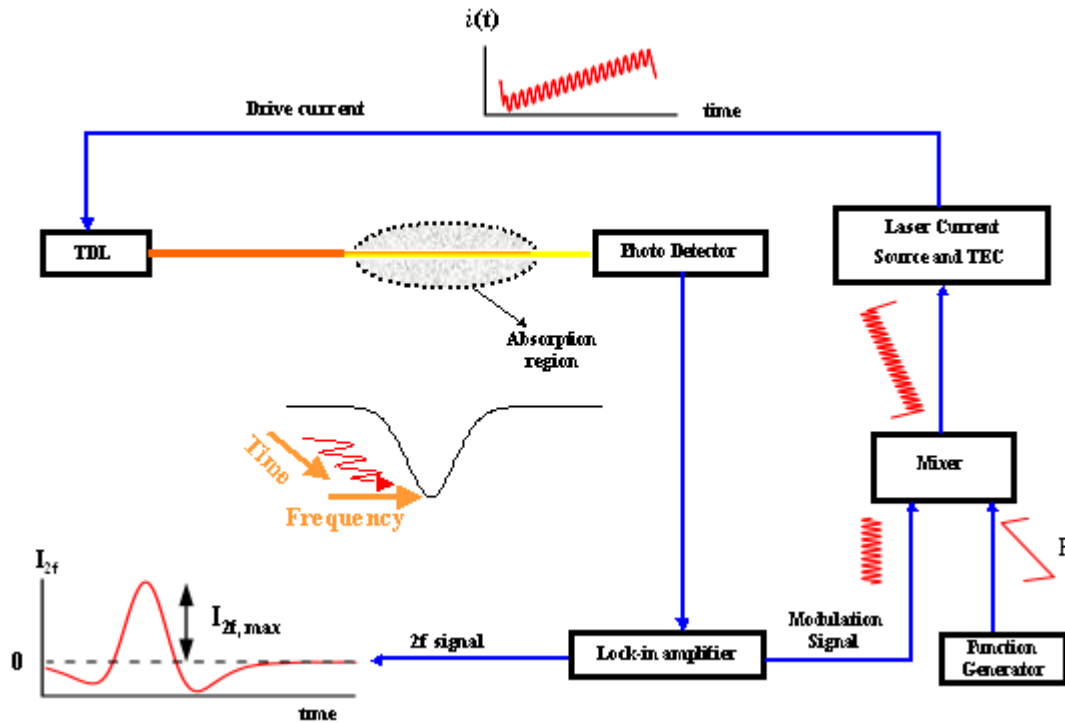
Figure 2.2: Typical experimental setup for wavelength modulation spectroscopy (from M. Gharavi)

The WMS technique allows for sensitivity improvement of 2-3 orders of

magnitude over direct absorption (Reid and Labrie 1981). Other advantages include

harmonic detection that nearly eliminates background, and frequency-domain

multiplexing to minimize source noises (fluid, combustion, or electronic) and separate

multiple laser signals. Multiplexed lasers can be carried to the diagnostic region on a

single multimode fiber, launched, and detected on a single detector.

Tunable diode lasers have been employed in the laboratory using direct

absorption and WMS to measure H_2O (Arroyo and Hanson 1993; Gharavi and Buckley

2004), CH_4 (Nagali, Chou, Baer, Hanson, and Segall 1996; Gharavi and Buckley 2005),

CO_2 (Mihalcea, Baer, and Handon 1998), and CO (Mihalcea, Baer, and Hanson 1997).

In industrial processes, multiplexed tunable diode lasers have successfully measured

multiple species (typically CO and H_2O) in high temperature atmospheric pressure

environments. Examples include electric arc furnaces (Nikkari, Di Iorio, and Thomson

2002), basic oxygen furnaces (Alendorf, Ottesen, Hardesty, Goldstein, Smith, and

Malcomson 1998), and coal fired power plants (Teichert, Fernholz, and Ebert 2003).

Xiang Liu at Stanford recently used a tunable diode laser sensor to measure gas turbine

exhaust temperature (2006). The industrial studies have all used direct absorption with

the exception of Nikkari. Liu's work is of particular interest since it is closely related to

this research. He methodically designed, constructed, laboratory-validated, and

demonstrated the use of a two TDL system to monitor two separate H_2O transitions and

calculate temperature in the exhaust of a 20 MW industrial gas turbine. Liu reported

temperature accuracies of better than than 5 K from 350 to 1000 K and sensor response to

changes in gas turbine load. A key improvement made by the research presented in this

thesis is the use of a single TDL to monitor two H_2O peaks for temperature and

concentration calculation.

2.4 Wavelength Modulation Spectroscopy Theory

Several researchers have created theoretical models to quantify WMS. Wahlquist

(1961) derived an analytical formula for the first three harmonic components of a

modulated Lorentzian absorption line. Wilson (1963) used numerical integrations to

obtain the first three harmonics for Lorentzian and Gaussian line shape functions. Using

a different mathematical approach, Arndt (1965) was able to generalize Wahlquist's

formula for all harmonic components. Reid and Labrie (1981) were the first to validate

these theoretical models with experimental data. Up until the 1990's, all the theoretical

models were based on wavelength modulation and did not account for intensity

modulation that results from the modulation of laser current in diode lasers. Philippe and

Hanson (1993) included intensity modulation effects in WMS but did not account for the

change in laser intensity as it is tuned across an absorption transition. A general

theoretical model was presented by Shilt (2003) for diode laser WMS for Lorentzian line

shape functions. In 2004, Gharavi formulated a general theoretical model for WMS

quantification especially applicable for combustion measurements. His model, used for

this research, can be used for any line shape function and includes all intensity

modulation effects.

If injection current i of a diode laser is modulated at frequency f as shown in

Equation 2.3:

$$i(t) = i_O + \Delta i \cos \omega t \, , \qquad\qquad (2.3)$$

where i_O is the DC offset, Δi is the amplitude of the current modulation, and ω is the

angular frequency ($\omega = 2\pi f$) then the modulation in the incoming laser current

simultaneously creates a modulation in the laser light intensity and in the optical

frequency v as shown in Equation 2.4 and Equation 2.5:

$$I(t) = \bar{I} + \Delta I \cos \omega t \, , \qquad\qquad (2.4)$$

$$v(t) = \bar{v} - \Delta v_m \cos(\omega t + \psi) \, , \qquad\qquad (2.5)$$

where $I(t)$ is the laser light intensity as a function of time, $\bar{I}$ is the average laser light intensity, and ΔI is the amplitude of the intensity modulation, and where $v(t)$ is the optical frequency as a function of time, $\bar{v}$ is the laser center frequency, Δv_m is the wavelength modulation amplitude, and ψ is the phase difference between the intensity modulation and the frequency modulation.

The wavelength modulation amplitude is one-half of the peak-to-peak difference in frequency of the laser light from the lowest point to the highest point in the injection current driving the laser. Equations 2.3 to 2.5 are applicable when the wavelength modulation amplitude, Δv_m, is relatively small (less than 0.12 cm^{-1}) since there is a linear relationship between laser intensity and optical frequency. This is the case when the high frequency sine wave modulation is the sole source of modulation of the laser drive current. However, in WMS where the laser is swept at a low frequency (typically up to 1 cm^{-1}) in addition to the high frequency signal modulation, the nonlinearity in laser intensity becomes apparent. The low frequency current signal causes the laser intensity to vary parabolically as shown in Equation 2.6:

$$I_0(\bar{v}) = I_0\left\{1 + s_{F1}(\bar{v} - v_0) + s_{F2}(\bar{v} - v_0)^2\right\} \qquad (2.6)$$

where I_0 is the laser intensity at some particular reference frequency (molecular absorption frequency, v_0 and s_{F1} and s_{F2} are coefficients with units of 1/cm^{-1} and 1/cm^{-2}, respectively. s_{F1} and s_{F2} are used to fit the observed interaction between intensity and frequency for a laser with sweep frequency, F. The superposition of the higher frequency sine wave current modulation adds another term and is expressed by:

$$I_0(\bar{v}) = I_0 \left\{ 1 + s_{F1}(\bar{v} - v_0) + s_{F2}(\bar{v} - v_0)^2 - s_f \Delta v_m \cos \omega t \right\} \quad (2.7)$$

where s_f is the laser intensity frequency parameter at modulation frequency f with

units of $1/\text{cm}^{-1}$. s_{F1}, s_{F2}, and s_f are highly dependent on the laser injection current

frequency.

The Beer-Lambert Law is used to convert the laser intensity modulation to species

concentration as expressed in Equations 2.1 and 2.2. Usually WMS is applied in

situations with small absorbance ($\alpha(v) < 0.1$). In this case a Taylor series expansion can

be used to approximate the Beer-Lambert law. The first two terms in the Taylor series

expansion of the exponential in Equation 2.1 give:

$$I(v) = I_0(v)\left[1 - \alpha(v)\right] \quad (2.8)$$

When the transmitted light $I(v)$ is detected by a wide bandwidth photodetector, the

photodetector generates a voltage signal proportional to $I(v)$ given by Equation 2.9:

$$V_P(\bar{v}) = K_P \left[1 + s_{F1}(\bar{v} - v_0) + s_{F2}(\bar{v} - v_0)^2 - s_f \Delta v_m \cos \omega t \right] \\ \times \left\{ 1 - \alpha[\bar{v} - \Delta v_m \cos(\omega t + \psi)] \right\} \quad (2.9)$$

where K_P is the electro-optical (or opto-electrical) gain of the photodetector in volts.

The electro-optical gain is the ratio of photodetector voltage to intensity. Expressing the

photodetector signal in a Fourier series gives:

$$V_P(\bar{v}) = K_P \left[\sum_{m=0}^{\infty} a_m(\bar{v}) \cos(m\omega t) + \sum_{m=0}^{\infty} b_m(\bar{v}) \sin(m\omega t) \right] \quad (2.10)$$

The nth harmonic component of the in-phase signal from the lock-in amplifier is

given by:

$$I_{n,p}(\bar{v}) = K_{P,L} \int_{-\pi}^{\pi} \left\{ \begin{bmatrix} 1 + s_{F1}(\bar{v} - v_0) + s_{F2}(\bar{v} - v_0)^2 - s_f \Delta v_m \cos \omega t \end{bmatrix} \\ \times \{1 - \alpha[\bar{v} - \Delta v_m \cos(\omega t + \psi)]\} \cos(n\omega t + \theta) \right\} d(\omega t) \quad (2.11)$$

The absorbance, $\alpha(v)$ in Equation 2.11 is given by:

$$\alpha(\bar{v}) = \alpha[\bar{v} - \Delta v_m \cos(\omega t + \psi)] = S(T)g_v[\bar{v} - v_0 - \Delta v_m \cos(\omega t + \psi)]Lp_{abs} \quad (2.12)$$

Equation 2.11 relates the measured $I_{n,p}(\bar{v})$ to the absorbing species partial pressure,

p_{abs}. The line shape can be represented by a Voigt function to account for the Doppler

and pressure broadening effects common in combustion applications. The Voigt function

$g_v(v - v_0)$ is defined by the following equations:

$$g_v(v - v_0) = AB(x, y) \quad (2.13)$$

where $A = \dfrac{1}{\Delta v_G}\sqrt{\ln(2)/\pi} \quad (2.14)$

$$B(x, y) = \frac{y}{\pi} \int_{-\infty}^{\infty} \frac{e^{-t^2}}{y^2 + (x-t)^2} \, dt \quad (2.15)$$

$$x = \frac{v - v_0}{\Delta v_G}\sqrt{\ln(2)} \quad (2.16)$$

$$y = \frac{\Delta v_L}{\Delta v_G}\sqrt{\ln(2)}. \quad (2.17)$$

and $g_v(v - v_0)$ has units of $1/cm^{-1}$, Δv_L is the pressure broadening half-width in cm^{-1},

Δv_G is the Doppler broadening half-width, v_0 is the frequency of the absorption

transition, and t is a variable of integration. The Doppler broadening half-width at half-

maximum depends upon the temperature and the molecular weight as shown in Equation

2.18:

$$\Delta v_G = 3.581 \times 10^{-7} v_0 \sqrt{\frac{T}{M}} \qquad (2.18)$$

where T is the temperature in Kelvin and M is the molecular weight.

The Voigt function is difficult to evaluate because of the integral in Equation 2.15 but can be approximated by Whiting's expression (Whiting 1968) as shown in Equation 2.19:

$$\sigma_V(v) = G(v_0)\left\{(1-x)e^{-0.693y^2} + \frac{x}{1+y^2} + 0.016(1-x)x\left[e^{-0.0841y^{2.25}} - \frac{1}{1+0.0210y^{2.25}}\right]\right\}$$

$$(2.19)$$

where $\quad x = \dfrac{\Delta v_L}{\Delta v_V} \qquad (2.20)$

$$y = \frac{|v - v_0|}{\Delta v_V} = \frac{|\bar{v} - v_0 - \Delta v_m \cos(\omega t + \psi)|}{\Delta v_V} \qquad (2.21)$$

Δv_V is the Voigt function half-width at half-maximum and can be calculated using the equation presented in (Olivero and Longbothum 1977):

$$\Delta v_V = 0.5346\Delta v_L + (0.2166\Delta v_L^2 + \Delta v_G^2)^{0.5} \qquad (2.22)$$

where Δv_L is the pressure broadening half-width at half-maximum solved using:

$$\Delta v_{L,j} = P\sum_i \chi_i \gamma_{i-j}, \qquad (2.23)$$

where $\Delta v_{L,j}$ is the pressure broadening half-width of molecule j, P is the total pressure in torr, χ_i is the mole fraction of molecule i, and γ_{i-j} is the pressure broadening coefficient with units of cm^{-1}/torr for a collision between i and j. Equation 2.23 thus sums the pressure broadening caused by all collision partners.

$G(v_0)$ in Equation 2.19 is the cross-section at absorption line center given by

Equation 2.24 as:

$$G(v_0) = \frac{S(T)}{2\Delta v_V \left(1.065 + 0.447x + 0.058x^2\right)} \qquad (2.24)$$

with units of cm^2.

As the Lorentzian or Gaussian half-width approaches zero, the Voigt function is

converted to a Gaussain or Lorentzian line shape respectively.

CHAPTER 3: Experimental Setup

3.1 Introduction

This chapter covers the lab and field setup done to support the TDL system gas turbine exhaust flow testing. In the laboratory, support hardware for the TDL lasers was manufactured along with glass and metal calibration cells to provide the spectroscopic data necessary to quantify temperature, H_2O, CO_2, and CO concentrations. For field-testing, the TDL system was packaged for industrial use and window assemblies were created to sample exhaust stack data. The field-testing also included setup of an FTIR system to gather data in parallel to the TDL system.

3.2 TDL Laser Selection

The initial plan was to develop a high-speed multi-gas sensor for use in commercial energy generation applications such as stationary gas turbines. The sensor, based on commercially available tunable diode lasers, was envisioned to measure NO, CO, CH_4, and H_2O simultaneously. Laser path-averaged temperature would also be calculated using the H_2O signal. Several researchers including Gharavi and Buckley (2005) had demonstrated H_2O and CH_4 TDL measurements in the past. Research done for this thesis found that the NO signal was too weak for quantification given the spectral range of commercially available TDL technology. CO and CO_2 were developed instead for TDL measurements presented in this thesis. The TDL gas turbine exhaust data was taken using the H_2O and CO_2 lasers since the CO concentrations present were too low to be quantifiable.

The line strengths of H_2O, CO_2, CO, CH_4, NO, and NO_2 transitions from 1500 to 8000 wavenumbers (6,667 to 1,250 nm) are shown in Figure 3.1. The data is from the Hitran 2004 database (Rothman et al. 2005) at 450 K, the gas turbine exhaust stack temperature.
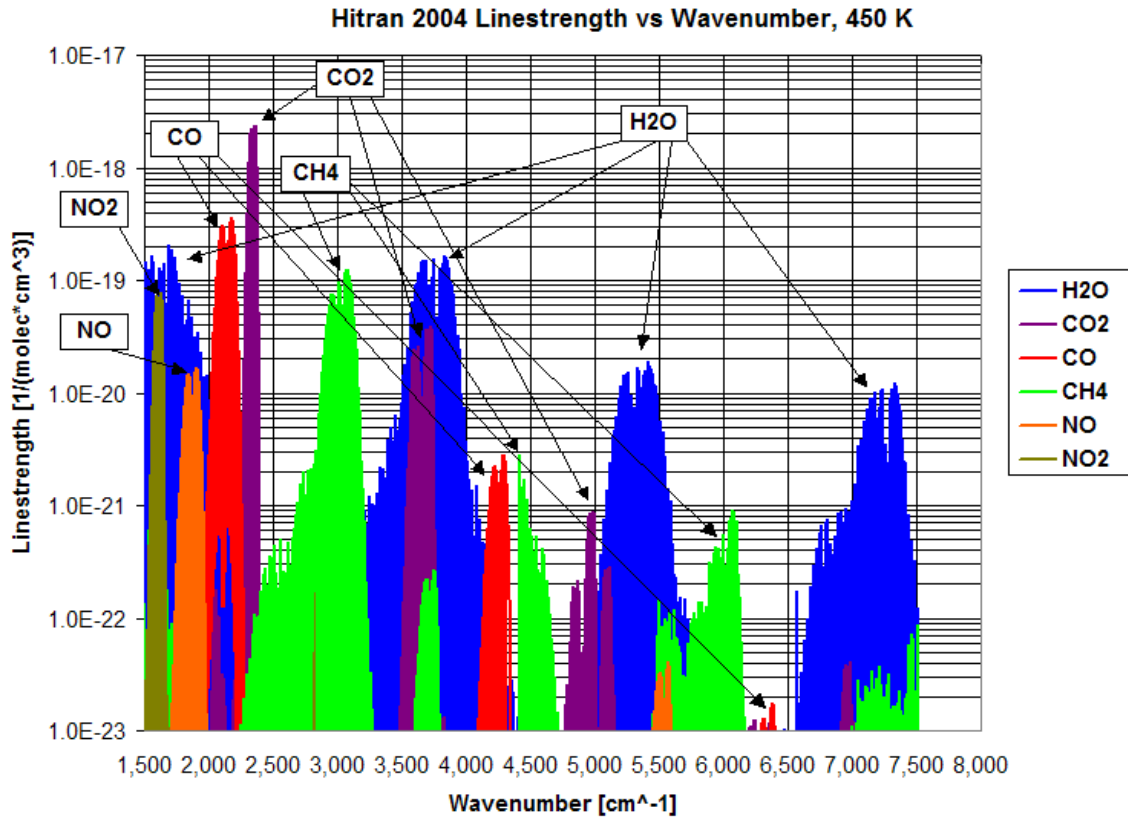
Figure 3.1: Line strength versus wavenumber for H_2O, CO_2, CO, CH_4, NO, NO_2 taken from the Hitran 2004 database at 450 K.

Tunable diode InGaAsP communication lasers operate in the near-infrared region between 5000 to 8333 wavenumbers (2,000 to 1,200 nm). H_2O dominates the near IR region. In the mid-infrared region, between 833 to 2500 wavenumbers (12,000 to 4,000 nm) CO_2, CO, H_2O, NO_2, and NO are strong. Table 3.1 lists detection limits for the strongest absorption peaks present in the mid and near-infrared regions.

Table 3.1: Detection limit at strongest absorption peaks in the mid- and near-infrared regions

Species	Mid-Infrared: Detection Limit^ (ppb)	Wavelength (nm)	Wavenumber (cm^-1)	Near-Infrared: Detection Limit^ (ppb)	Wavelength (nm)	Wavenumber (cm^-1)
H_2O	2.0	5,490	1821	60	1,390	7194
CH_4	1.7	3,260	3067	600	1,650	6061
CO	0.8	4,600	2174	30,000/500	1,570/2,330	6369/4292
CO_2	0.1	4,230	2364	3,000	1,960	5102
NO	5.8	5,250	1905	60,000/1,000	1,800/2,650	5556/3774
NO_2	3.0	6,140	1629	340	680	14706

^ Assuming 1e-5 absorbance, 1 Hz bandwidth & 1 meter path length
From Southwest Sciences website, http://www.swsciences.com/technology/sensors.html

For this research, TDL measurements were sought for NO, CO, and CO_2, along with H_2O and CH_4 which had already been proven. Multiple factors played a role in selecting the optimal TDL for a given species. The laser needed to be in a region where there was a strong absorption peak across the expected temperature range, which was free of interference from other species, and which was available as a low-cost commercial product. A target temperature of 450 K was chosen since this was the expected exhaust temperature from the stationary gas turbines at UCSD.

In the near-infrared region, where telecommunication TDLs exist, there is no strong absorption peak for NO. Strong NO features are present in the mid-infrared region, particularly at 1900 wavenumbers (5,250 nm), where Quantum Cascade (QC) lasers operate. Mann (2003) and Wehe (2003) have demonstrated promising results using these lasers. Unfortunately, QC lasers are not mass-produced and are currently quite costly. Some also require cryogenic cooling that adds significant complexity to the system. For these reasons NO was dropped from the experimental measurement plan.

Evaluation of the Hitran 2004 database showed that the 6380 to 6400 wavenumber region was promising for CO measurement since this was the highest

absorption region in the near-infrared range. A distributed feedback (DFB)

telecommunication TDL was obtained at 6391 wavenumber (1,565 nm). As shown in

Figure 3.2, this spectral region is free of H_2O and CO_2 interference from 300 to 900 K.

CH_4 also has no spectral features in this region. The effects of temperature broadening

were also investigated using Hitran data. The peak line strength at 6391 wavenumber

was exhibited at 450 K, the target temperature.
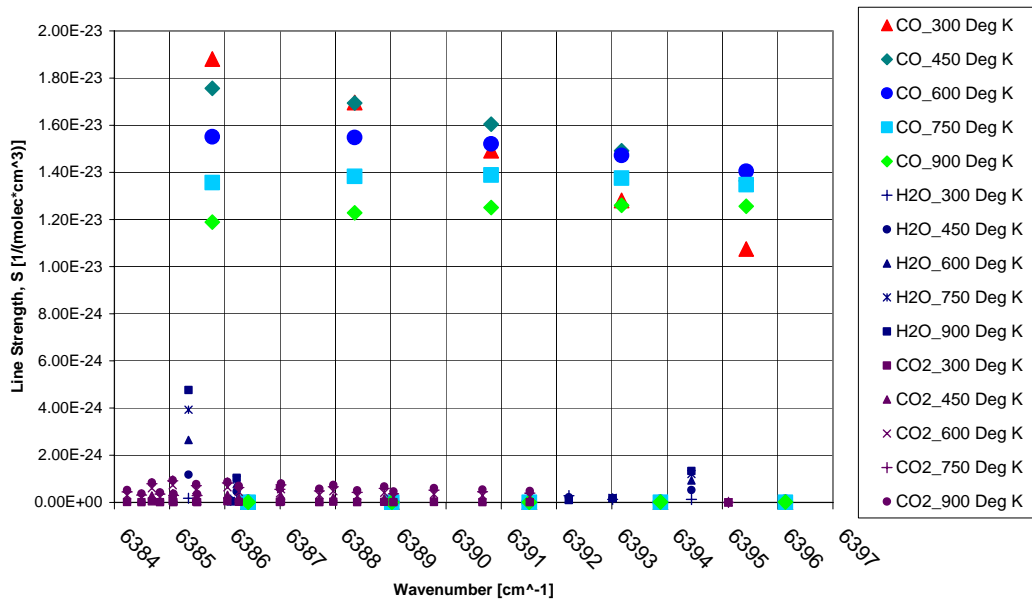
Figure 3.2: Hitran 2004 line strength versus wavenumber data from 300 to 900 K used to choose CO laser

A similar study was completed using Hitran 2004 data for CO_2. A distributed

feedback (DFB) telecommunication TDL was found at 6250 wavenumber (1,600 nm).

As shown in Figure 3.3, this wavenumber is free of CO interference from 300 to 900 K.

H_2O and CH_4 also had no spectral features in this region. The effects of temperature

broadening were also investigated using Hitran data. Like CO, the peak line strength at

6250 wavenumbers was exhibited at 450 K, the target temperature.
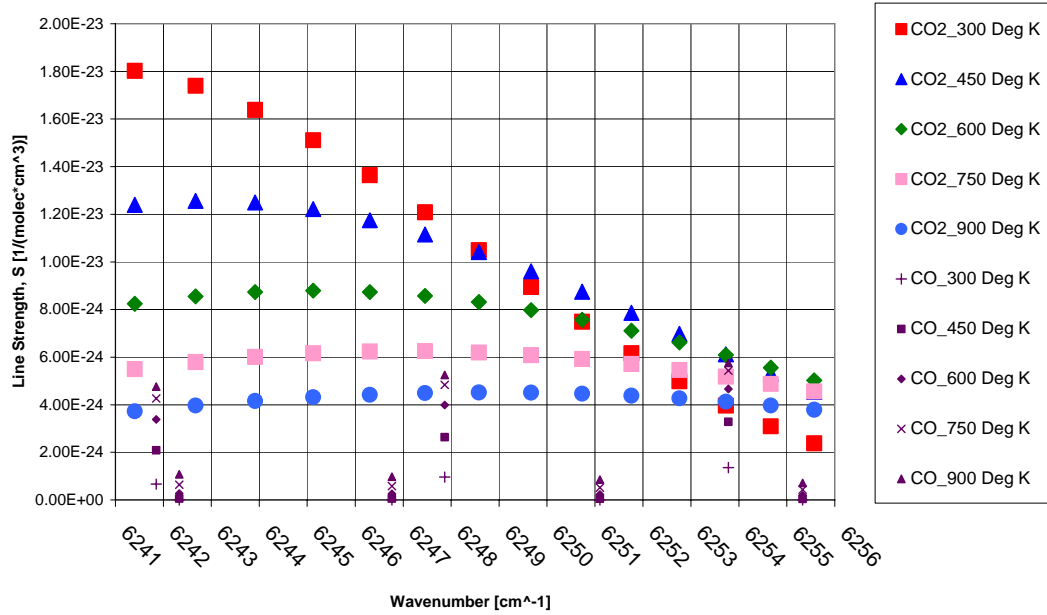
Figure 3.3: Hitran 2004 line strength versus wavenumber data from 300 to 900 K used to choose the CO_2 laser

Table 3.2 summarizes the DFB lasers used for this research. They are all 14 pin fiber-pigtailed telecommunication lasers with costs ranging from $500 to $1200 for a single laser.

Table 3.2: DFB lasers used for this research

Species	Wavelength (nm)	Wavenumber (cm^-1)	Manufacturer	Model Number	Power (mW)	Line Strength at 450 Deg K [1/(molec*cm^3)]
H_2O	1,477	6771	Corning Lasertron	QLM4S781-050	2	1.20E-22
CO	1,565	6391	Lucent Laser	D2570T916	40	1.60E-23
CO_2	1,600	6250	NTT Electronics	P873	20	8.74E-24
CH_4	1,651	6057	OKI	OL6109L-10B	10	7.70E-22

Figure 3.4 shows where the lasers operate in the near-infrared spectrum at 450 K based on the Hitran data. The line strength of CH_4 decreases with increasing temperature while the line strength of H_2O increases. The line strengths of CO_2 and CO are not dependent on temperature (or exhibit very weak dependence) over this temperature range. This is shown in Figure 3.5.
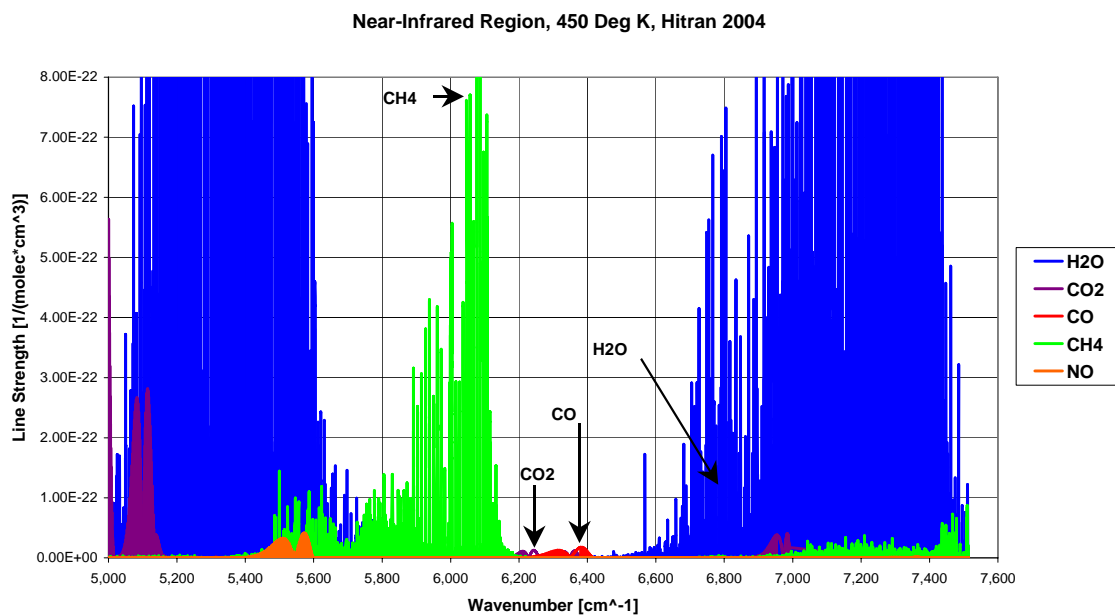
Figure 3.4: Line operating region of the lasers used in this research along with NO taken from Hitran 2004 at 450 K
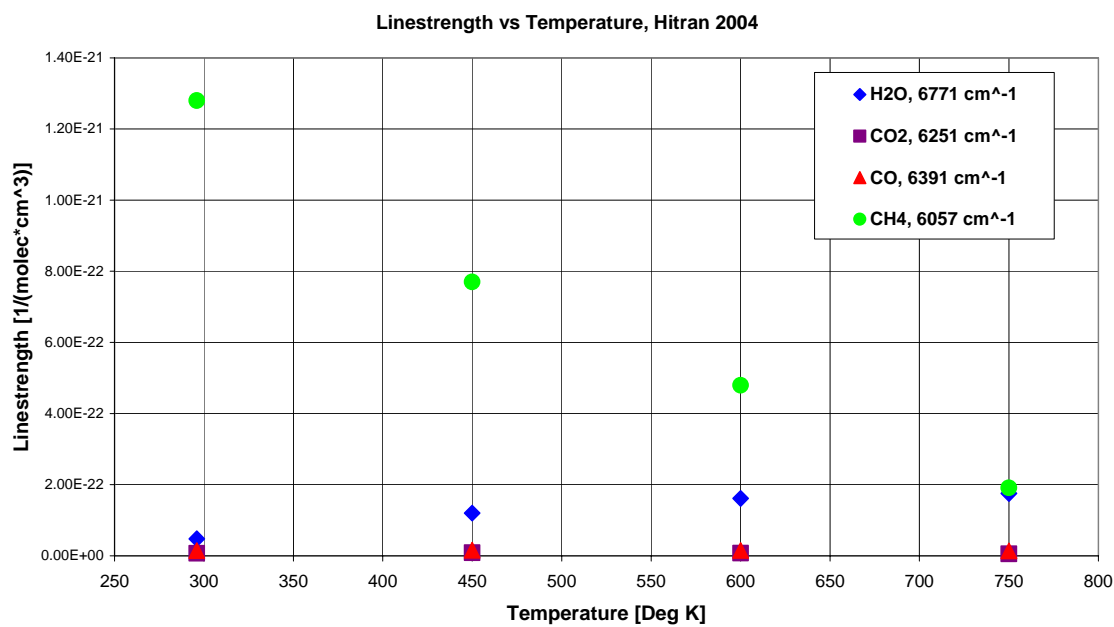
Figure 3.5: Line strength as a function of temperature for the H_2O, CO_2, CO, and CH_4 lasers

3.3 Laboratory Setup

Multiple devices were constructed to gather the necessary spectroscopic information required for quantification of H_2O, CH_4, CO, CO_2, and temperature using TDL's. Electrical cables were made to control the lasers and a 4-laser mounting plate was created. The fiber optic cabling to and from the lasers was also arranged. In order to conduct the experiments, new glass and metal cells were designed and manufactured. The details of these assemblies will be presented in this section.

The four lasers are all room temperature, single mode, fiber pig-tailed DFB TDLs with 14 pin butterfly style pin-outs. These lasers have on-board thermoelectric cooling for temperature control. Four special cables were soldered to connect the lasers to the laser controllers (ILX Lightwave Model LDC-3900) using two-15 pin female connectors for the laser end and a 9-pin male connector to interface with the laser controller. A wiring diagram is shown in Figure 3.6. A metal base plate was also manufactured to situate up to four lasers.

To gather H_2O-related data for the 2nd harmonic spectra model as well as the temperature-dependent line strength and pressure broadening parameters, a new longer glass cell was designed without the need for argon purging. The previously existing glass cell, shown in Figure 3.7, is 30 cm in length and uses argon purging to prevent atmospheric H_2O from interfering with the laser beam before and after the cell in the transition zones outside of the ceramic heater.
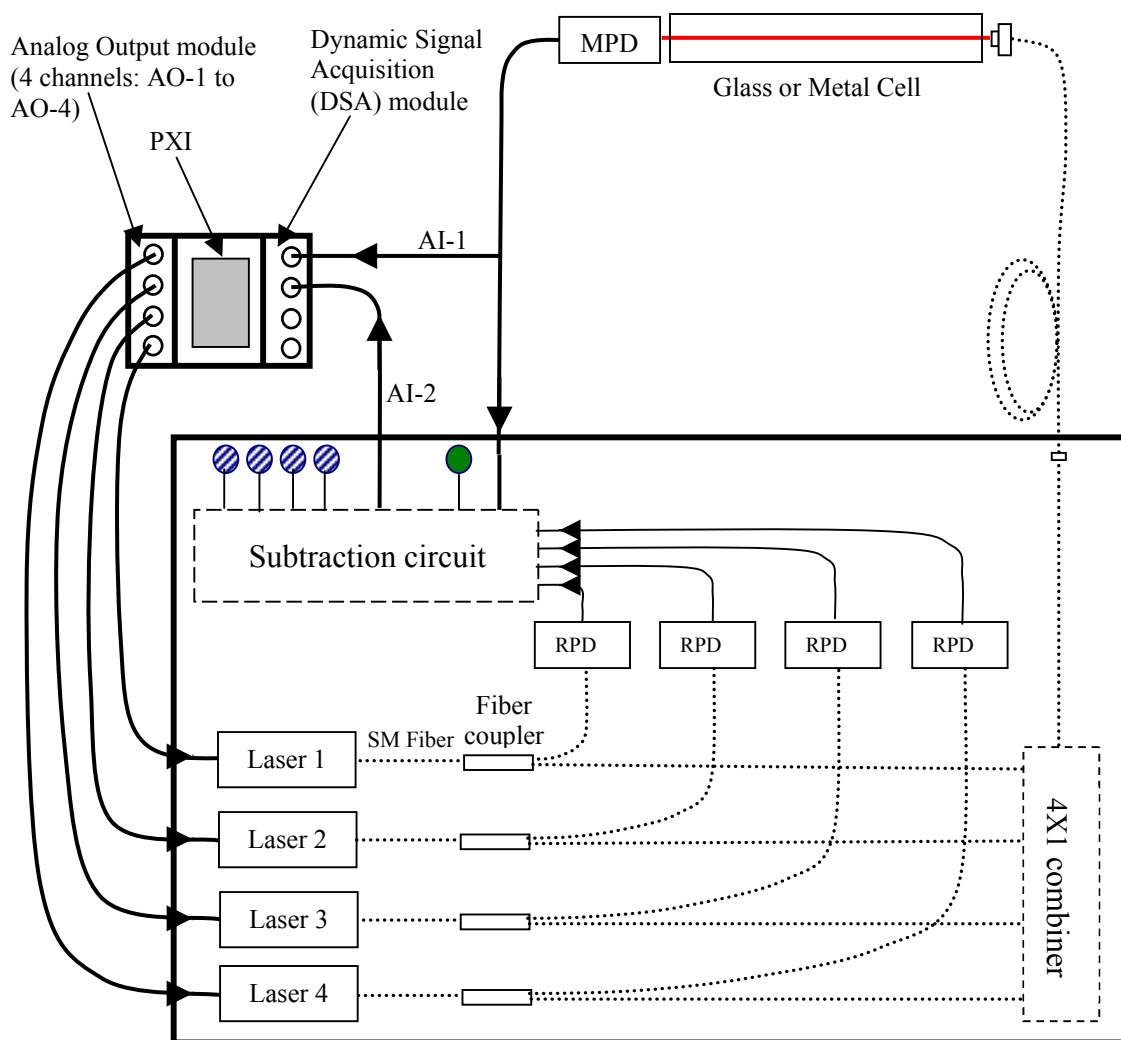
Adjustment knob for adjusting the gain of the Reference Photodetector (RPD)

Adjustment knob for adjusting the gain of the Main Photodetector (MPD)

······ Optical signal

—— Electrical signal

AI-1: This channel is used by the LabVIEW™ program to calculate first harmonic components of each absorption signal based on the MPD signal.

AI-2: This channel is used by the LabVIEW™ program to calculate second harmonic components of each absorption signal based on the subtracted signal.

AO-1 to 4: These channels are used by the LabVIEW™ program to generate four modulation signals, which drive the lasers.

Figure 3.6: Laser, cable, and laser controller wiring diagram (portion from A. Schuger)
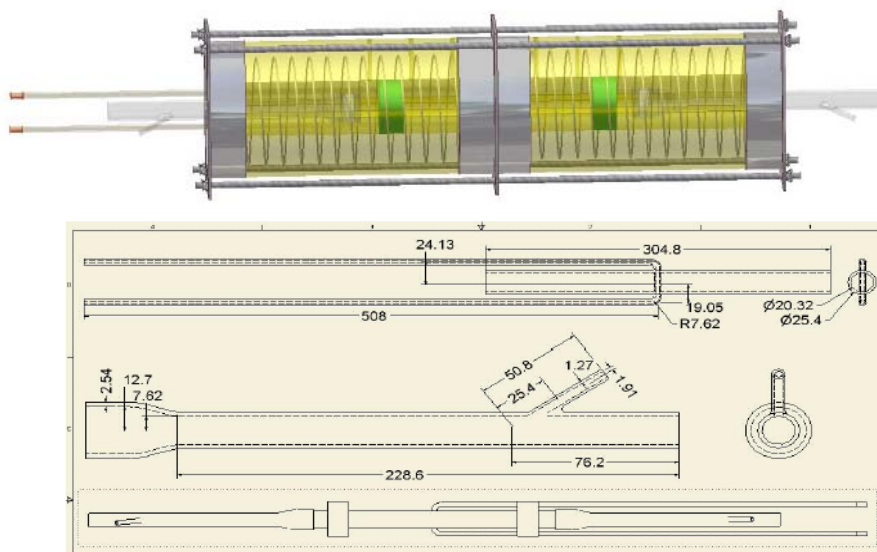
Figure 3.7: Existing 30 cm core glass cell designed by M. Gharavi

The new glass cell core is 40 cm long instead of 30 cm and utilizes a three-chamber design so that the outer two chambers can be brought to vacuum, which eliminates the need for argon purge. Four 1-inch diameter 1-degree fused silica wedge windows create the three sections and prevent back reflection of the laser light. The design drawing is shown in Figure 3.8. Two ¼-inch diameter tubes join the center chamber for species input/evacuation and pressure sensing. The new longer glass cell still mounts in the existing ceramic heater housing. Along with the new glass cell, two more 30 cm cells were made to support future testing. Curtis Technologies, a company located in Sorrento Valley, manufactured all of the glasswork.
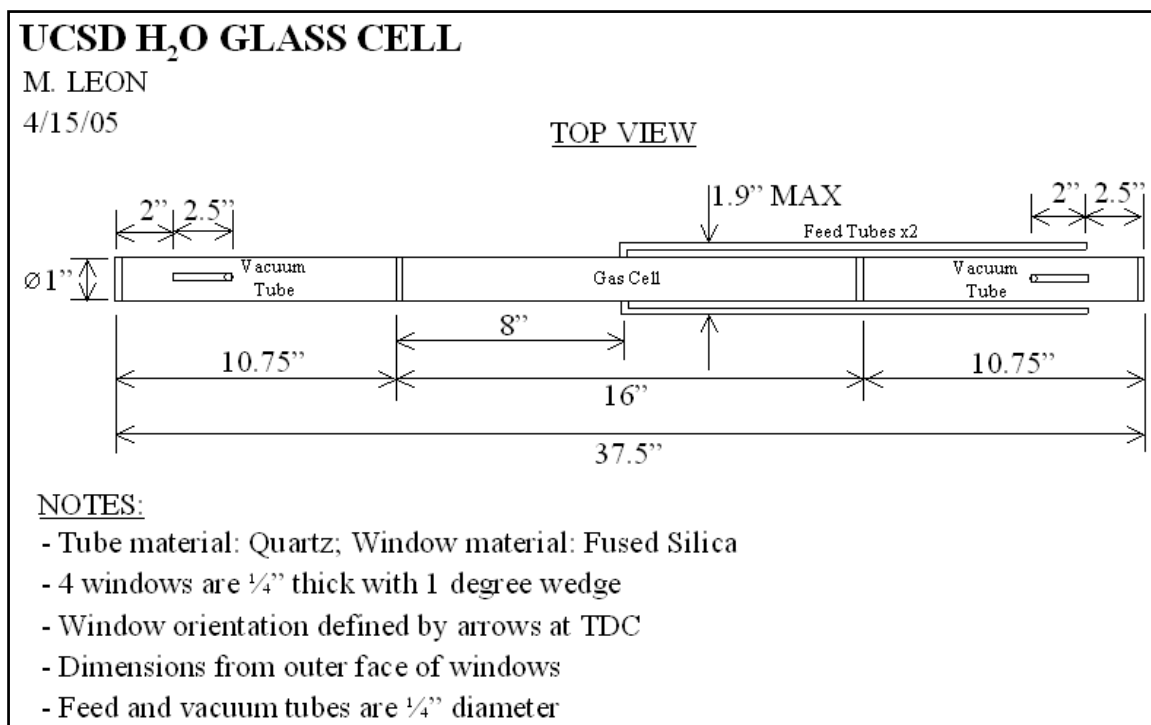
Figure 3.8: Four-window 40 cm long core glass cell created for this project

To achieve the larger path length needed to detect CO and CO_2, two 1-meter long 1.5-inch diameter metal cells were designed and constructed. Each 1-meter long stainless steel cell is housed within insulated ceramic heaters that extend 21 cm past either side of the cell. Two 30 cm long glass vacuum tubes eliminate interference from atmospheric water vapor allowing the laser-collimating lens and photo detector to be placed away from the high temperature inside the cell. Six K-type TC's measure the gas temperature along the axial length of the cell. A modular approach was taken to allow for access to the windows for cleaning. Metal C-Seals made by Perkin-Elmer were used to provide the seal between the metal flange and fused silica window. Two metal cells were constructed so that one could be used for low pressure testing and the other for high pressure flow-through testing.

The 1.5-inch diameter 1-meter long metal cell uses 2-inch diameter 1-degree wedge windows to prevent reflection interference (etaloning) along with the two 30 cm long vacuum tubes that have 1-inch diameter 1-degree wedged windows on each end. The laser beam must travel through 6 windows over 1.6 meters. Due to the wedged windows, while the laser passes through the 1-meter long metal cell, the beam could be offset up to 27.5% of the inner diameter of the metal cell. This is calculated from Equation 3.1 where q_d is the deviation of a ray incident on a wedged window with a wedge angle α.

$$q_d = (n-1)\alpha \qquad\qquad (3.1)$$

A value of 1.5 was used as the refractive index, n. Additionally, to ensure that the beam passed through the entire path without interference, each 1-degree wedge window was oriented such that walk-ff of the beam was avoided.

The C-Seals™ used in the seals are metal-to-metal seals able to create a gas-tight metal seal due to flexure of the seal under compression. These were required instead of elastomer-type seals due to the service temperature of the gas cell. For each application, the C-Seals are different due to their orientation; the positive curvature (convex) side is designed to go toward the lower pressure. Made of Inconel 718 with gold plating, they have a maximum operating temperature of 1400°F and can be used in ultra high vacuum (10^{-10} Torr) to high-pressure (200,000 psi) applications.

The crux of the metal cell design is the wedge window-to-flange interface. For the low-pressure metal cell, the C-Seal is oriented facing outward as shown in Figure 3.9. The wedge window was modified to have a flat rim, which allows for a parallel seal. The same methodology was used for the high-pressure metal cell but the flange was machined

differently to account for the inward facing C-Seal as shown in Figure 3.10. The wedge

window machining information is shown in Figure 3.11.
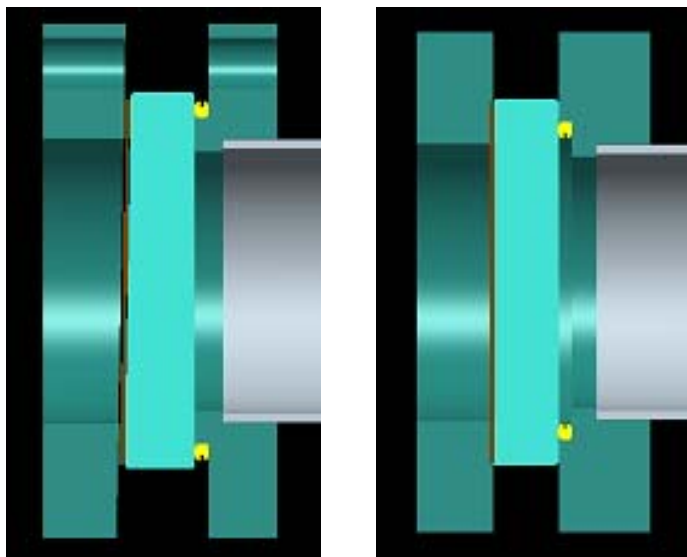
Figure 3.9: Left: Low-pressure metal cell wedge window-flange interface (note outward facing C-Seal)

Figure 3.10: Right: High-pressure metal cell wedge window-flange interface (note inward facing C-Seal)
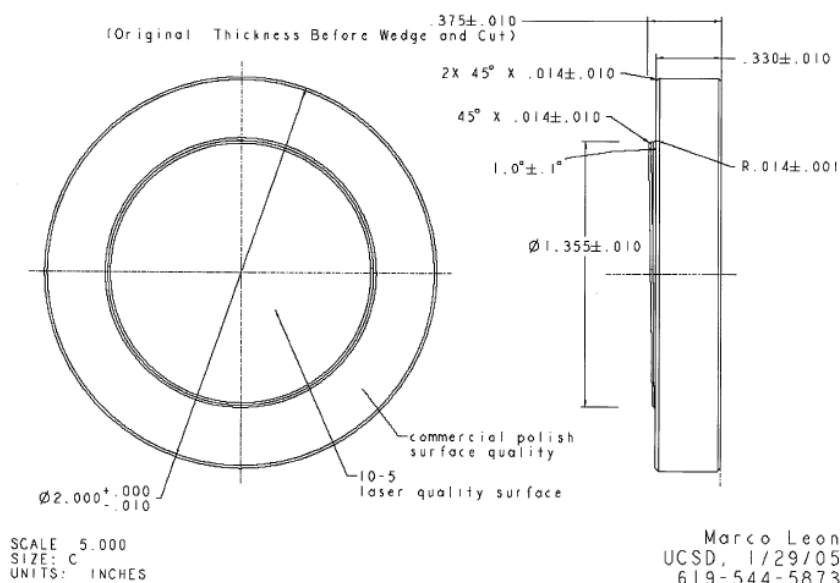
Figure 3.11: Wedge window machining drawing

The main body of the metal cell is seamless 1.5 inch outer diameter stainless steel 304 tubing (0.049 inch wall thickness). The inside window-to-window length is 1 meter. Six 0.062-inch diameter probe Conax fittings with graphoil seals good to 925°F are welded to the tube to seal and allow depth control of the K-type thermocouples (TCs). From the end of the tube, which has a total length of 39.072 inches, they are located at the following axial positions: 4.786, 11,536, 16.786, 22.036, 27.286, and 34.286 inches. The low-pressure metal cell has two ¼-inch Swagelok 90° fittings welded on for species feed/evacuation and pressure sensing. Along with one ¼-inch Swagelok 90° fitting for pressure sensing the high-pressure metal cell has two ½-inch Swagelok 90° fittings on either end to support flow-through testing. Pro-E models of the low and high-pressure metal cells are shown in Figures 3.12 and 3.13.

The thermocouples are K-type, inconel-sheathed, 6 feet long, and 0.063 inch diameter. The sensing side is sealed and the junction is ungrounded to provide electrical isolation. Mini male connectors were used on the opposite end. Three sets of 20-inch long 240V semi-cylindrical 5-inch ID Watlow ceramic fiber heaters encase the metal cell (9 inch OD). The heaters are covered with 1-inch thick mineral wool insulation and sheet metal. The feed/suction, pressure lines, and TCs all exit the ends of the heater assembly, which are enclosed with 1-inch thick silica insulation board. The entire metal cell/heater assembly was modeled using Pro-E and is shown in Figure 3.14. The bill of materials for the system, including vendor and part number information is listed in the Appendix. The glass and metal cell assemblies cost $10,300. Bruce Thomas (Laboratory Engineer) and Alan Yang (Undergraduate Student) completed the majority of the fabrication in-house.
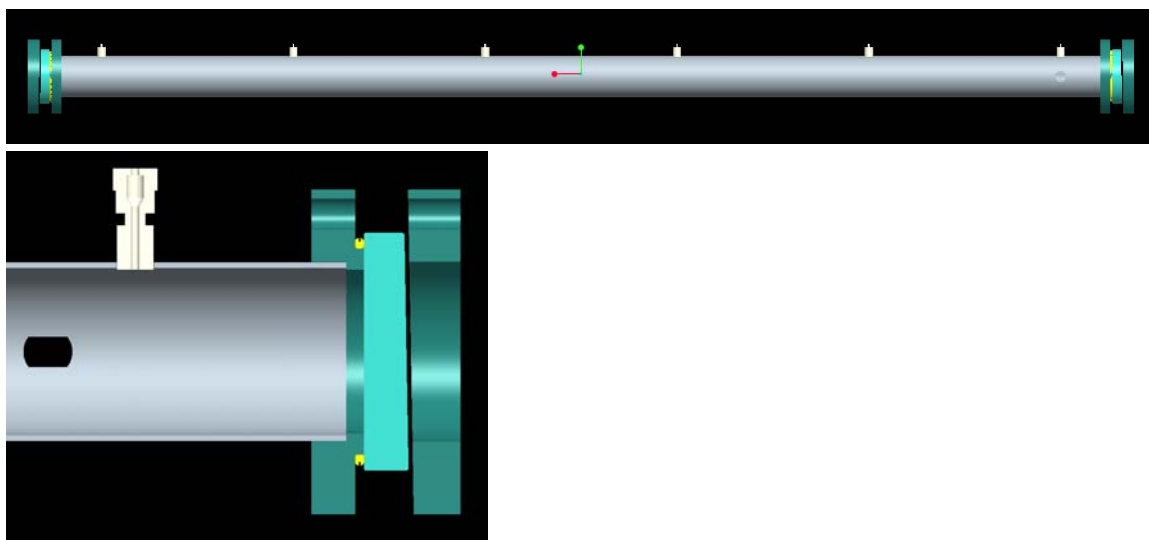
Figure 3.12: Low-pressure metal cell assembly
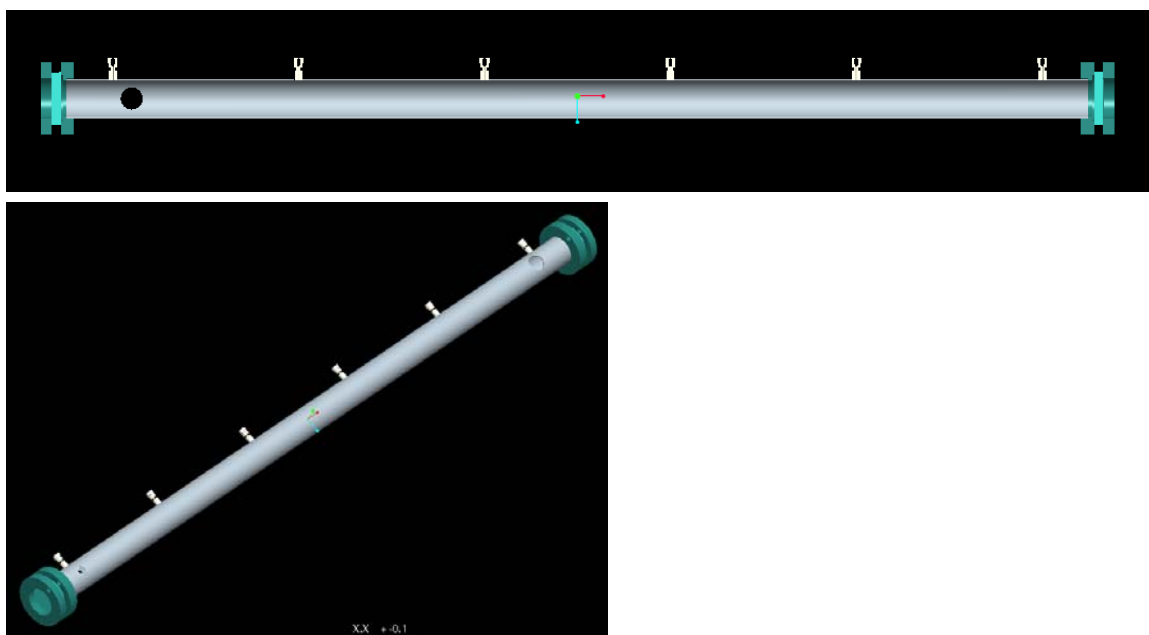
Figure 3.13: High-pressure metal cell assembly
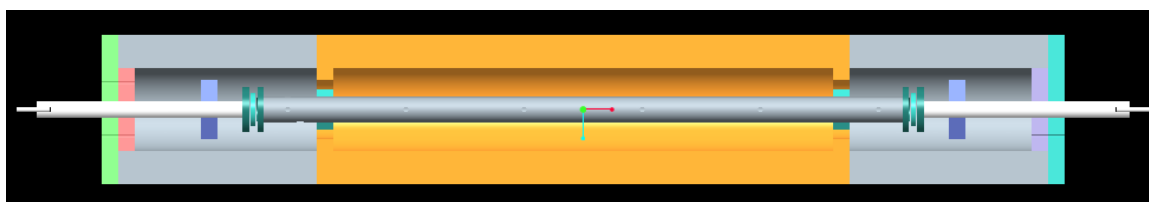
Figure 3.14: Metal cell & heater assembly modeled using Pro-E; the 30 cm long glass vacuum tubes are also shown on each end (note: actual heaters used were three 20-inch long sections, not two 12-inch and one 32-inch heater in the middle as shown)

Testing with both the glass and metal cell is essentially the same; the metal cell is used for elevated pressure experiments. A diagram of the single-species measurement setup is shown in Figure 3.15 with the static cell being either the glass or metal version. Temperature regulation in the metal cell is done independently by the three sets of cylindrical heaters (zone heating). A TC from each section feeds three independent WATLOW series 93 DIN temperature controllers connected to three WATLOW DIN-A-MITE power controllers to regulate the current sent to the three sets of WATLOW cylindrical heaters. The glass cell system just uses one TC to control the single set of cylindrical heaters. A New Focus model 2033 large-area IR photodetector detects light passing through the cell. An MKS Baratron pressure transducer measures interior pressure.
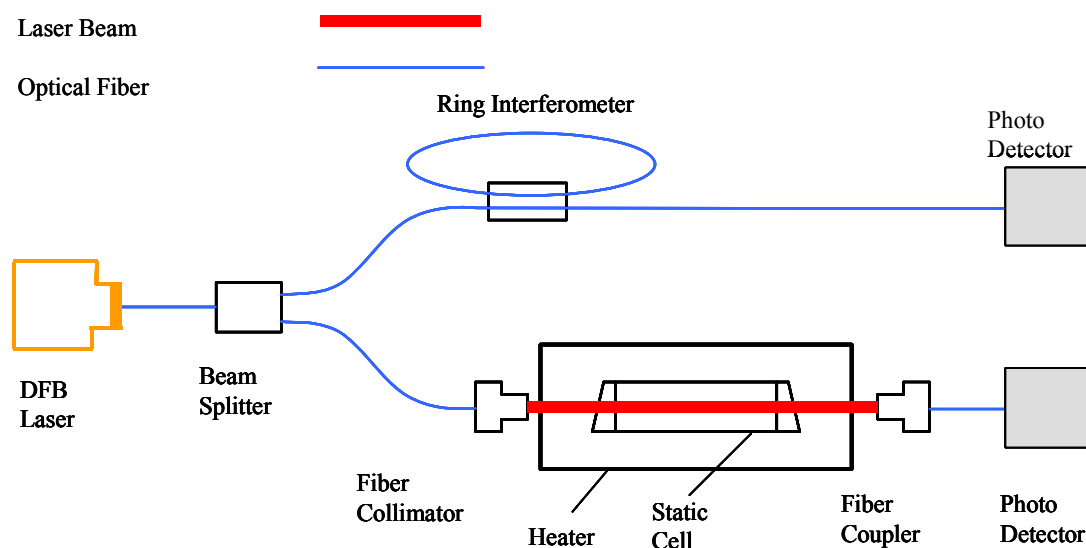
Figure 3.15: Single species TDL testing setup using the glass or metal static cell

The ring interferometer was made by M. Gharavi using a spliced 95/5 single mode directional fiber optic coupler with an approximate circumference of 30 cm.

The Free Spectral Range (FSR) of the ring interferometer can be calculated by Equation

3.2 (Stokes, Chodorow, and Shaw 1982):

$$Free\ Spectral\ Range = \frac{1}{\eta L} \qquad\qquad (3.2)$$

where η is the refractive index of the ring interferometer material and L is the optical

path length (cm). Assuming a refractive index of 1.5 for infrared light, the FSR is 0.022

cm^{-1}. Due to uncertainty of the exact length of the ring, the FSR was determined to be

0.022694 cm^{-1} by comparing the spectra of the ring interferometer signal to the

absorption spectra of two H_2O transitions whose frequencies are well known and

documented in the HITRAN database.

A series of hand valves was used to control the evacuation and then species

introduction to the cell. Up to four separate species could be added to the cell. Leakage

rate testing showed that the metal cell holds an acceptable vacuum, with a leakage rate of

0.035 Torr/hour. Pictures of the metal cell and gas system are shown in Figure 3.16.
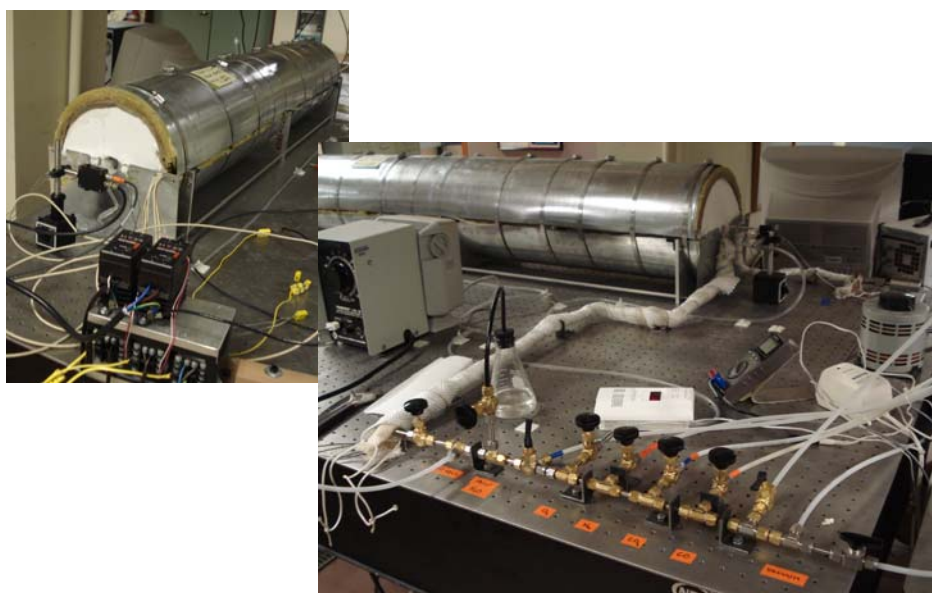
Figure 3.16: Pictures of the metal cell setup in the TDL laboratory

3.4 Field Setup

All of the laboratory work was aimed at demonstrating real-world monitoring of exhaust temperature, H_2O, and CO_2 content using a TDL system at the UCSD power plant. The setup for this field-testing is documented in this section.

UCSD has a utility plant to provide electrical power, heating, and cooling to the campus. Two Solar Turbines Incorporated, 14 MWe Titan 130 stationary gas turbines provide about 90% of the electrical power for the UCSD campus. Both engines are equipped with heat recovery and Selective Catalytic Reduction (SCR) SCONOx systems. The SCONOx system brings the NOx emissions down from sub 25 ppm to less than 3 ppm, which is the concentration that the plant is permitted to emit. A schematic and plant drawings for the gas turbine systems are shown in Figures 3.17 and 3.18.
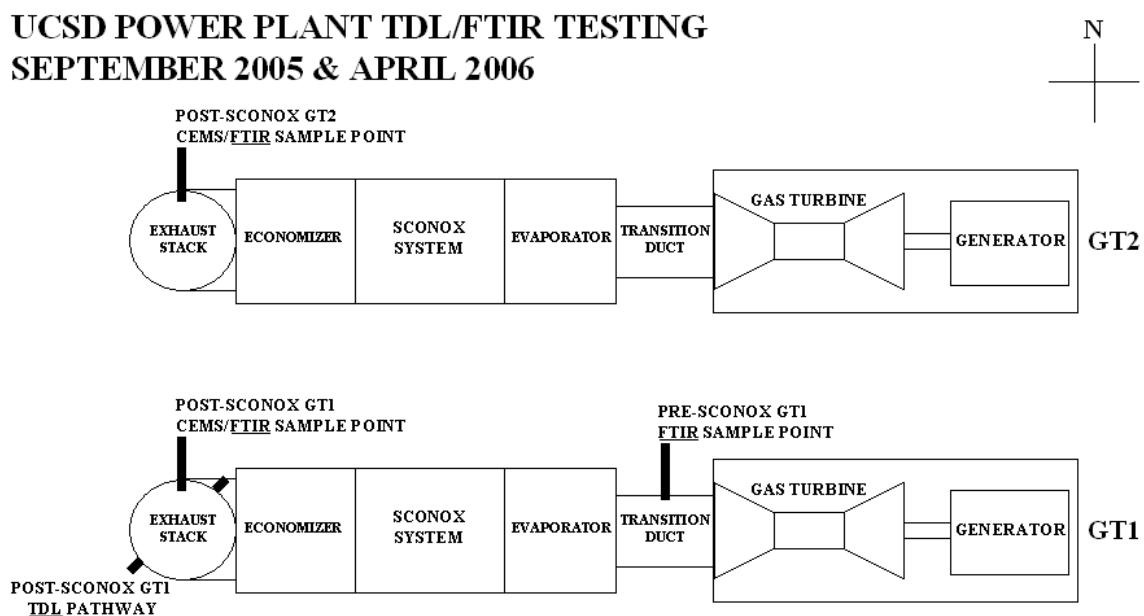
Figure 3.17: General top down view of UCSD power plant gas turbine systems
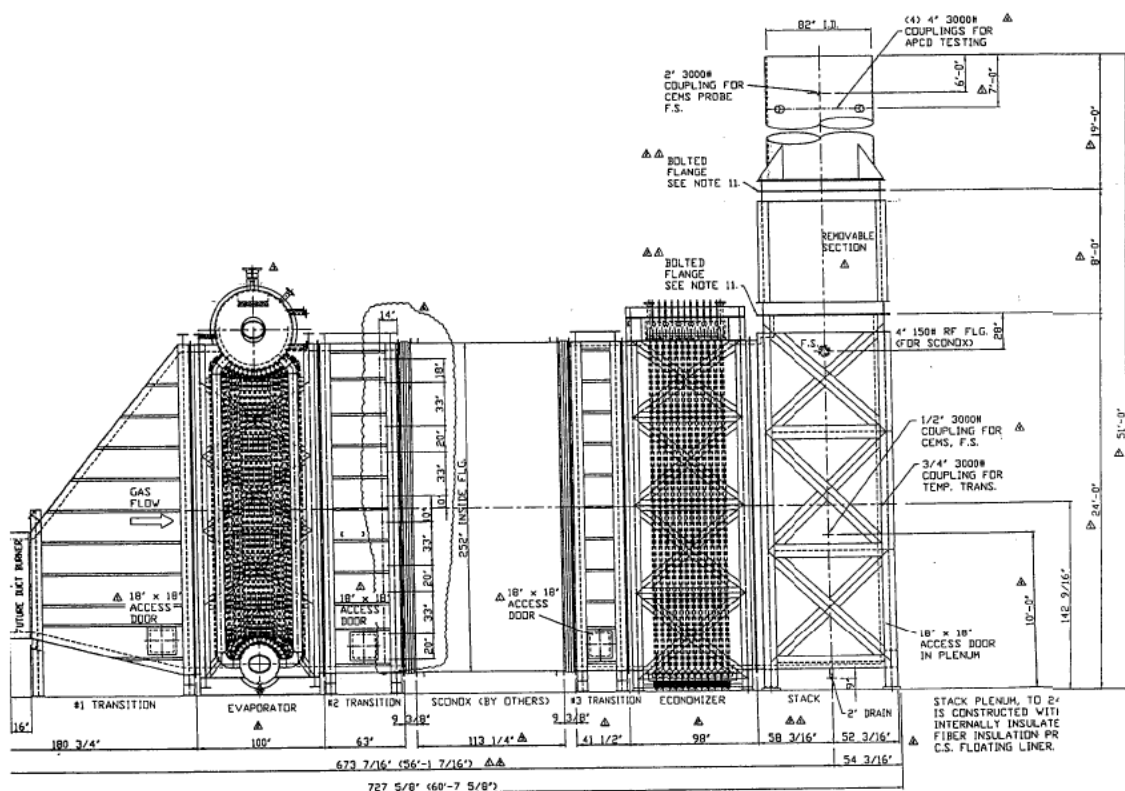
Figure 3.18: Side view of the systems downstream of each gas turbine (from J. Dilliot, UCSD power plant manager)

Field data was collected on two occasions. In September 2005, TDL and FTIR (Fourier-Tranform InfraRed, discussed below) data was taken over a six-day period for data comparison purposes. After improving the TDL system, TDL data was collected again in April 2006 over an eight-day period. The TDL system was set up on the GT1 (Gas Turbine 1) exhaust stack using custom-made window fixtures mounted to the 4-inch coupling ports used for air emissions testing for regulatory purposes. The FTIR sampled exhaust stack gas from the sample lines used by the on-site Continuous Emissions Monitoring System (CEMS) at the power plant. The CEMS collects NOx and O_2 data from each stack downstream of the SCONOx systems, switching from stack to stack every 7.5 minutes. Post SCONOx FTIR data was collected through the CEMS heated

hoses, sampling from the stack exhaust not being analyzed by the CEMS. The FTIR and
TDL systems were located in the temperature-controlled CEMS shack shown in Figure
3.19. The gas turbine operating data was collected every hour by Solar's Remote
Monitoring & Diagnostics (RM&D) system.

Figure 3.19: Left: GT1 exhaust stack and CEMS shack; Right: TDL system on top of FTIR

The FTIR (MKS model 2030) operates by analyzing a gas sample in 5.1-meter
long path length gas cell. The background and sample spectra are subtracted and then
compared to a library of reference spectra to quantify concentration data for CO_2, H_2O,
CO, NO, NO_2, N_2O, H_2CO, CH_4, and CF_4. A separate analyzer was used to determine
the concentration of O_2, as the FTIR cannot measure homonuclear diatomic molecules

because they have no dipole. FTIR data was logged every minute with 4 cm^{-1} resolution.

A fresh fill of LN_2 was required every 12 hours to provide cooling for the detector.

The TDL window assemblies located in the exhaust stack were constructed just

like the high-pressure metal cell ends. A 2.5-inch long section of 1.5-inch diameter

tubing was welded to a window assembly flange while the other side was welded to a 4-

inch male NPT plug. Once installed, each assembly was wrapped with insulation. The

insulation was necessary to prevent condensation buildup inside the wedge window. This

approach avoided having to purge the windows. L-shaped brackets were mounted to

each flange to support the TDL collimating lens or photodetector. Pictures of the two

windows are shown in Figure 3.20.

Figure 3.20: Left: TDL collimating lens window assembly (note the CEMS sample hose in the background); Right: TDL photodetector window assembly

The TDL system consists of a laser controller, a Labview PXI computer, portable

TDL box housing the lasers, associated conditioning circuitry, and calibration

interferometer, and monitor/mouse/keyboard. The system is shown in Figure 3.21. A

schematic of the TDL box is shown in Figure 3.22. For the field-testing only two of the

available four channels were used (H_2O and CO_2).

Figure 3.21: TDL system located inside the UCSD power plant CEMS shack

Figure 3.22: TDL box schematic (portion from A. Schuger)

CHAPTER 4: Conversion of TDL Data

4.1 Introduction

This chapter will cover quantification of the WMS output signal for temperature and concentration measurements. The focus will be on temperature, H_2O, and CO_2, since these were the measurements made in the field. A summary of the procedure used for the concentration calculations will be presented.

4.2 H_2O, CO_2, and Temperature WMS Conversion

As explained in Section 2.4, the WMS output signal, $I_{n,p}(\bar{v})$, can be related to an absorbing species concentration by Equation 2.11.   Even (rather than odd) harmonics are used since $I_{n,p}(\bar{v})$ is maximum at the absorption center for the even harmonics. The main hurdle in quantification using this equation is that the line shape function must be known. This implies that the concentration of all of the important collisional species and the temperature are known. By characterizing all laser parameters and the spectroscopic parameters of the absorption transition, the $I_{n,p}(\bar{v})$ per unit absorbing species concentration can be calculated through Equation 2.12. The concentration of the measured absorbing species is calculated by dividing the peak of the measured $I_{n,p}(\bar{v})$ signal by the peak of the calculated $I_{n,p}(\bar{v})$. Since prediction of the electro-optical gain K_P is difficult, it can be determined by comparing a set of measured $I_{n,p}(\bar{v})$ signals at known concentrations and temperatures with the corresponding calculated values from Equation 2.12. Temperature can be determined by the ratio of two integrated absorption

lines from a single species when the line strengths of the two transitions vary with temperature.

Gharavi's (2004) model simulates the WMS second harmonic spectra of the H_2O and CO_2 lasers and is used to convert laser absorption data to temperature and concentration. The C++ code takes into account the changes in laser intensity that accompany WMS, the phase difference between intensity modulation and wavelength modulation, and the effects of pressure broadening and temperature broadening. The model requires the following inputs:

- Mole fraction of reactants;
- Laser operating parameters;
- Line strength fitting parameters; and,
- Broadening coefficient fitting parameters.

The mole fraction of reactants is determined from the flow rate of the reactants. The mole fraction of the combustion species in the application to gas turbine combustion is based on a complete combustion approximation. The laser operating parameters are measured and include: the modulation depth, Δv_m, intensity-frequency parameters (s_{F1}, s_{F2}, and s_{f1}), and electro-optical gain K_P. The modulation depth was calculated by the C++ code with an initial guess corresponding to the following expression,

$$\Delta v_m = \frac{\# \, fringes * FSR}{2} \qquad (4.1)$$

where $\# \, fringes$ is the number of fringe points in the high-frequency signal from the modulation depth measurements and FSR is the free spectral range of the interferometer. A summary of the intensity-frequency parameters (s_{F1}, s_{F2}, and s_{f1}), and electro-optical gain K_P for the H_2O and CO_2 lasers is shown in Table 4.1.

Table 4.1: H_2O and CO_2 spectroscopic data

Laser	S_{F1}	S_{F2}	S_{f1}	K_p
H_2O	-1.528	-0.017	-3.56	23.0
CO_2	-1.078	-0.247	-1.941	87.0

The line strength fitting parameters are obtained through least-squares fitting of the calculated line strengths versus temperature from the HITRAN database for all of the selected transitions. Pressure broadening measurements were done to calculate pressure-broadening coefficients for all of the quenching species. The glass cell was used in the laboratory to characterize the spectroscopic properties of H_2O and CO_2 using the direct absorption technique. The metal cell was used to quantify pressure broadening using the WMS technique. A team of undergraduate students led by Alan Yang and Chris Hartley completed this work.

Given these inputs the following steps were necessary for quantification of temperature and concentration of H_2O and CO_2.

1. Measure the 2nd harmonic signal for H_2O transitions and calculate the ratio of the two peaks, $R_{I,II} = I_{2f}^{H2O}(v_I) / I_{2f}^{H2O}(v_{II})$ as illustrated in Figure 4.1.
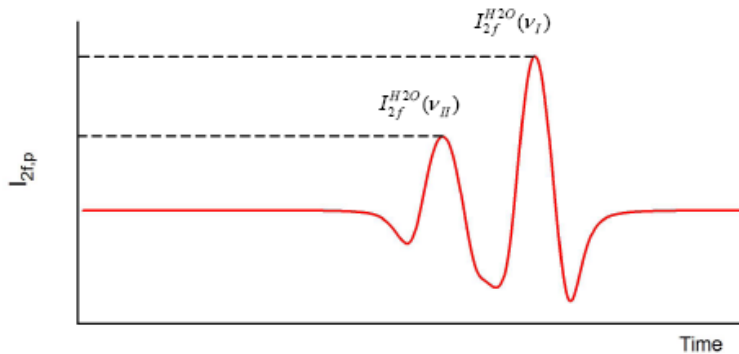
Figure 4.1: Typical 2nd harmonic signal of H_2O at the selected H_2O transitions (from Gharavi 2004)

2. Measure the 2nd harmonic signal peak for the CO_2 transition, $I_{2f}^{CO2}(v_0)$
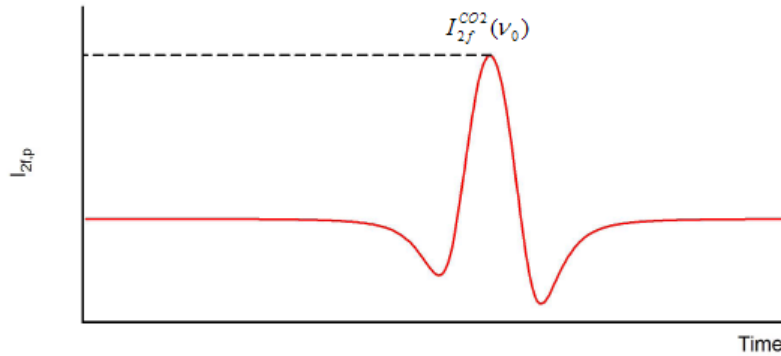
Figure 4.2: Typical 2nd harmonic signal of CO_2 at the selected CO_2 transition

3. Use the measured $R_{I,II}$ and pre-calculated HITRAN $R_{I,II}$ versus temperature correlation to calculate temperature, T_m. The correlation is shown in Figure 4.3.
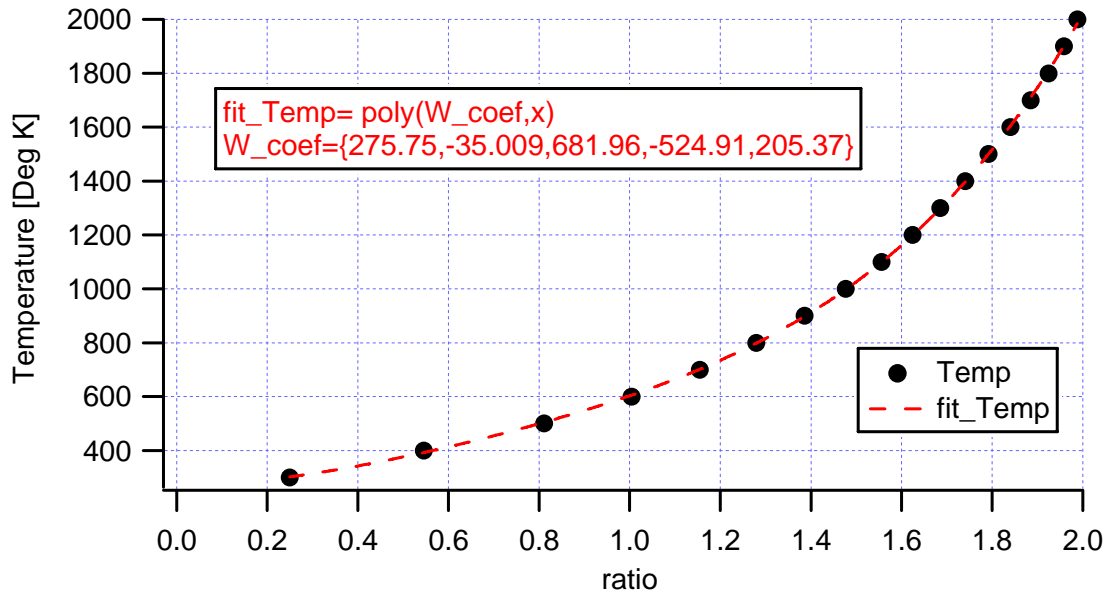
Figure 4.3: Temperature versus $R_{I,II}$ (ratio) data for the selected H_2O transitions from the HITRAN database

4. Laboratory-generated metal cell data on the variation of one of the H_2O peaks in the 2nd harmonic spectra $\hat{I}_{2f}^{H2O}(v_I)$ with temperature is used to calculate

$\hat{I}_{2f}^{H2O}(v_I)$ at T_m. Note that the $\hat{I}_{2f}^{H2O}(v_I)$ versus temperature data is normalized by laser power and the partial pressure of H_2O.

5. Laboratory-generated metal cell data on the variation of the CO_2 peak in the 2nd harmonic spectra $\hat{I}_{2f}^{CO2}(v_0)$ with temperature is used to calculate $\hat{I}_{2f}^{CO2}(v_0)$ at T_m. Note that the $\hat{I}_{2f}^{CO2}(v_0)$ versus temperature data is normalized by laser power and the partial pressure of CO_2.

6. Calculate the partial pressure of H_2O by $P_{H2O} = K_p \dfrac{I_{2f}^{H2O}}{\hat{I}_{2f}^{H2O}(T_m)}$, where I_{2f}^{H2O} is the field-measured WMS 2nd harmonic peak normalized by the laser power. The field gas turbine exhaust concentration data was calculated using the following equation: $mole\_H2O = \dfrac{I2f\_H2O\_norm\_filtered}{200*2.725e-6*760*23.0}$. (4.2)

7. Calculate the partial pressure of CO_2 by $P_{CO2} = K_p \dfrac{I_{2f}^{CO2}}{\hat{I}_{2f}^{CO2}(T_m)}$, where I_{2f}^{CO2} is the field WMS measured 2nd harmonic peak normalized by the laser power. The field gas turbine exhaust concentration data was calculated using the following equation: $mole\_CO2 = \dfrac{I2f\_CO2\_norm\_filtered}{200*6.050e-7*760*87.0}$. (4.3)

$I2f\_H2O\_norm\_filtered$ and $I2f\_CO2\_norm\_filtered$ in equations 4.2 and 4.3 are defined in Chapter 5. The numerical components of equations 4.2 and 4.3 correspond to $K_p \dfrac{1}{\hat{I}_{2f}^{H2O}(T_m)}$ and $K_p \dfrac{1}{\hat{I}_{2f}^{CO2}(T_m)}$ respectively.

CHAPTER 5: Field Test Results

5.1 Introduction

The results of the Gas Turbine, FTIR and TDL data gathered from the UCSD power plant will be presented in this chapter. The FTIR data was taken along with TDL data in September 2005 over a six-day period. After improving the TDL system, TDL data was collected again in April 2006 over an eight-day period. Temperature, H_2O concentration, and CO_2 concentration will be compared along with the error analysis results.

5.2 FTIR Field Data

The FTIR system was set up as described in Chapter 3. The data presented in this section is focused on the post-ScoNOx system exhaust stream results taken near the TDL system ports. Since the FTIR gas sample was taken from the same heated hose system as used by the CEMS system, FTIR data from both gas turbine units was collected, switching between units every 7.5 minutes. An overview of the setup and FTIR data collected is presented in Table 5.1 and 5.2. There were two main groups of data collected from the exhaust stack port, each covering approximately 1.5 days (data groups A and D as shown in Table 5.2).

Table 5.1: Table showing data collected from each gas turbine unit

	Stack:	Engine SN:	Notes:
South Unit (GT1)	1	0012L	FTIR/TDL/GT Data
North Unit (GT2)	2	0019L	FTIR/GT Data
Note: FTIR sampling from non-CEMS stack (ie. When CEMS is on stack 1, FTIR is sampling from stack2)			

Table 5.2: Table showing collected FTIR species and field data groups

Species	Units
CO	ppm
CO_2	%
NO	ppm
NO_2	ppm
N_2O	ppm
NOx	ppm
NOx corrected to 15% O2	ppm
H_2CO	ppm
H_2O	%
CH_4	ppm
CF_4	ppm
O_2	%

	Start	End	Data Group
Post SCONOX DATA			
	9/16/05 16:12	9/18/05 5:24	A
	9/19/05 16:53	9/19/05 16:57	B
	9/19/05 17:21	9/19/05 17:31	C
	9/20/05 18:00	9/22/05 8:50	D
Ambient Air			
	9/19/05 16:27	9/19/05 16:53	
	9/19/05 17:31	9/19/05 17:32	
	9/19/05 17:33	9/19/05 17:48	
Pre SCONOX DATA (GT1)			
	9/19/05 17:49	9/19/05 17:53	A
	9/19/05 17:58	9/20/05 17:51	B
Nitrogen			
	9/19/05 15:59	9/19/05 16:17	
	9/19/05 17:07	9/19/05 17:07	
	9/22/05 8:53	9/22/05 8:56	
	9/22/05 9:17	9/22/05 9:27	

The exhaust stack FTIR data along with the gas turbine hourly percent load data over a one-hour period from data group A is shown in Figure 5.1. It is interesting to note that GT1 emits higher levels of CO and CH_4 than GT2.

Figure 5.1: Complete FTIR data over a 1-hour time period noting that both exhaust stacks are sampled every 7.5 minutes (refer to Table 5.2 for FTIR species units)

UCSD Power Plant Post SCONOX FTIR Data
note: FTIR sampling switches from GT1 to GT2 in 7.5 minutes intervals

Figure 5.2: Overview of CO_2, H_2O, and CH_4 along with gas turbine percent load from FTIR data group A (9/16-9/18/05) (refer to Table 5.2 for FTIR species units)

UCSD Power Plant Post SCONOX FTIR Data
note: FTIR sampling switches from GT1 to GT2 in 7.5 minutes intervals
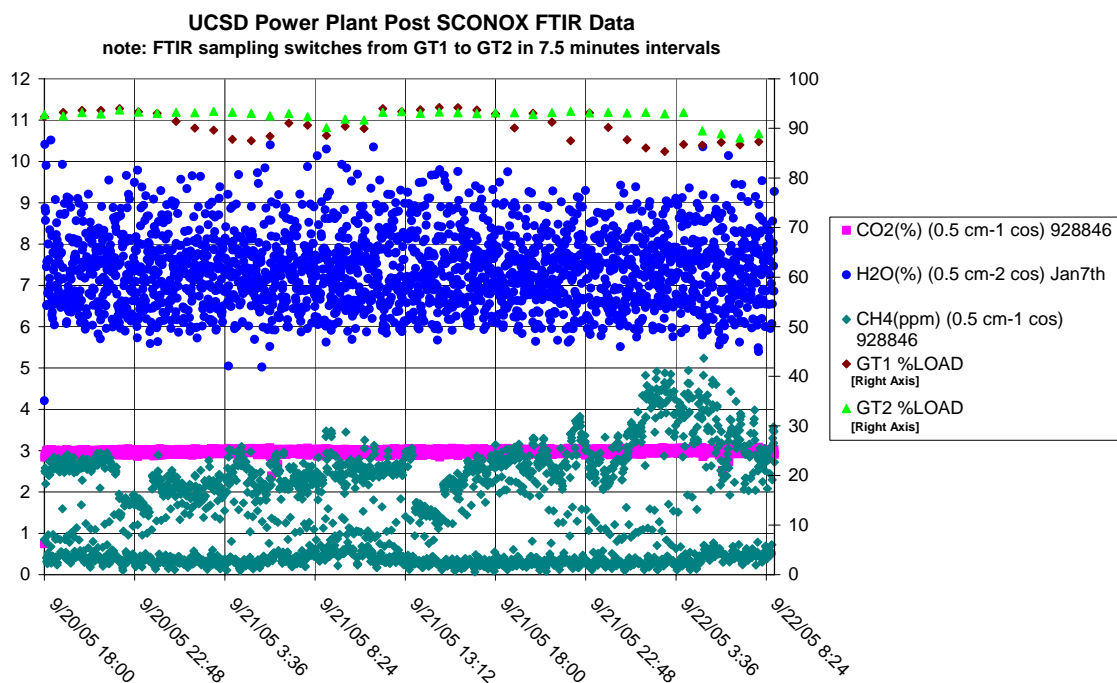
Figure 5.3: Overview of CO_2, H_2O, and CH_4 along with gas turbine percent load from FTIR data group D (9/20-9/22/05) (refer to Table 5.2 for FTIR species units)
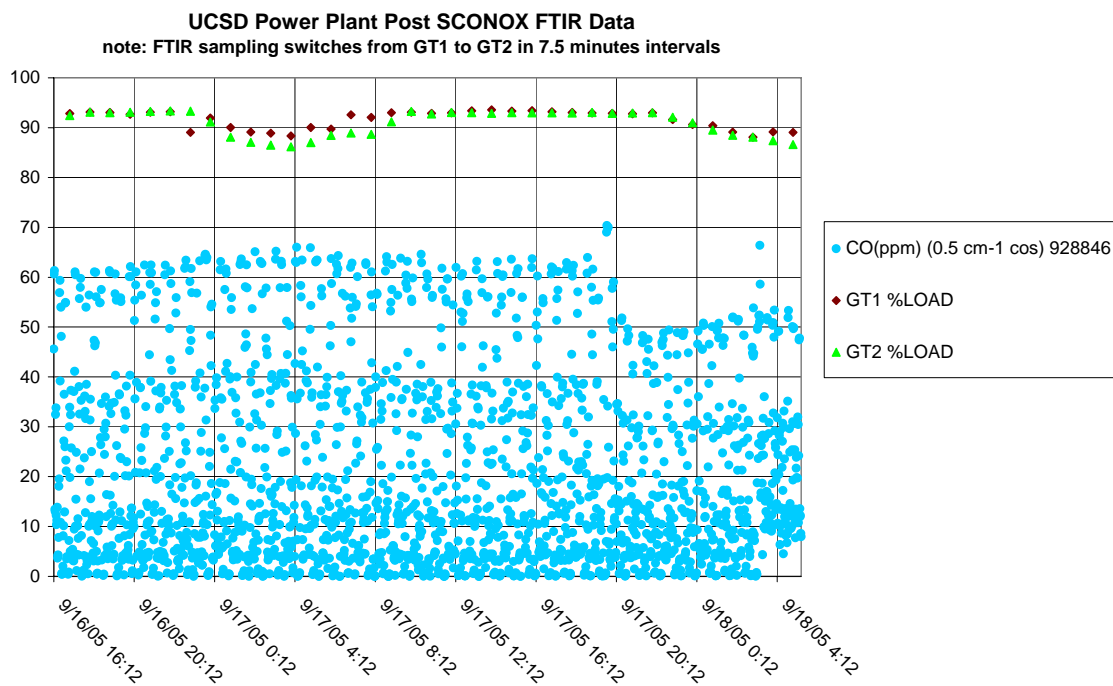
Figure 5.4: Overview of CO along with gas turbine percent load from FTIR data group A (9/16-9/18/05) (refer to Table 5.2 for FTIR species units)
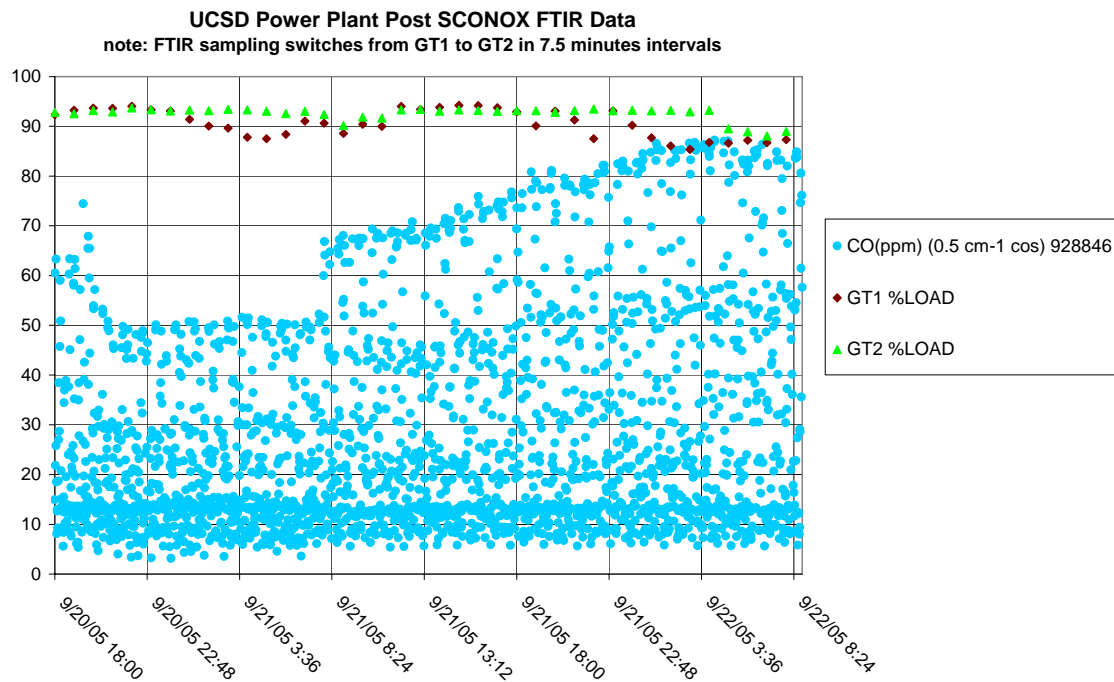
Figure 5.5: Overview of CO along with gas turbine percent load from FTIR data group D (9/20-9/22/05) (refer to Table 5.2 for FTIR species units)
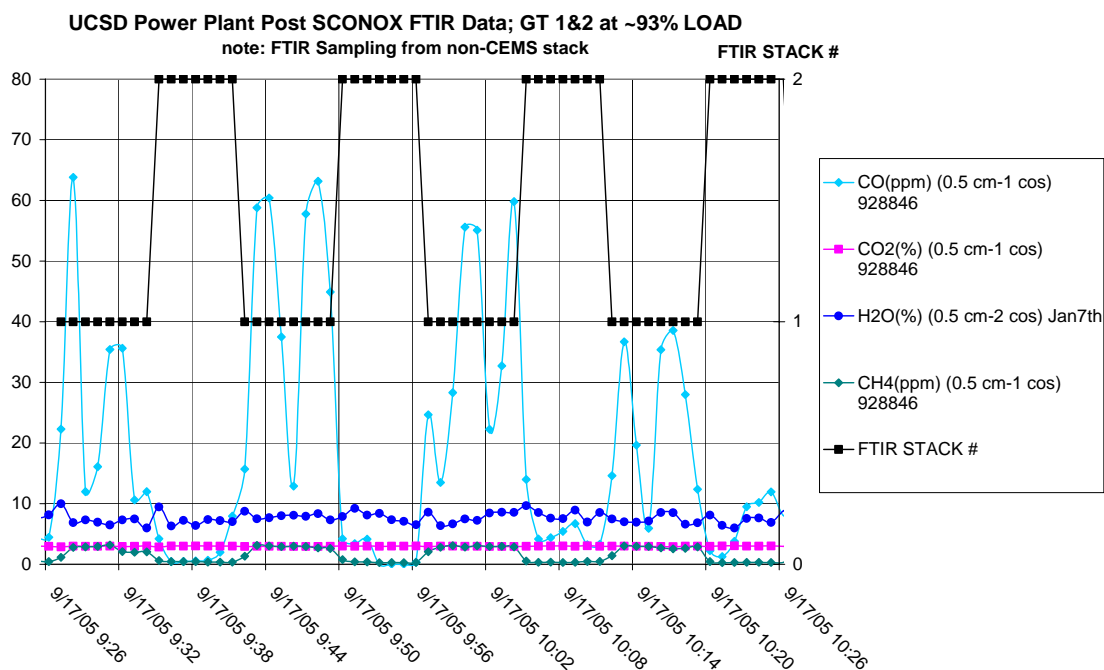
Figure 5.6: FTIR 1-hour time period from 9/17/05 showing CO, CO$_2$, H$_2$O, and CH$_4$ along with FTIR stack number; gas turbines operating close to 93% load (refer to Table 5.2 for FTIR species units)
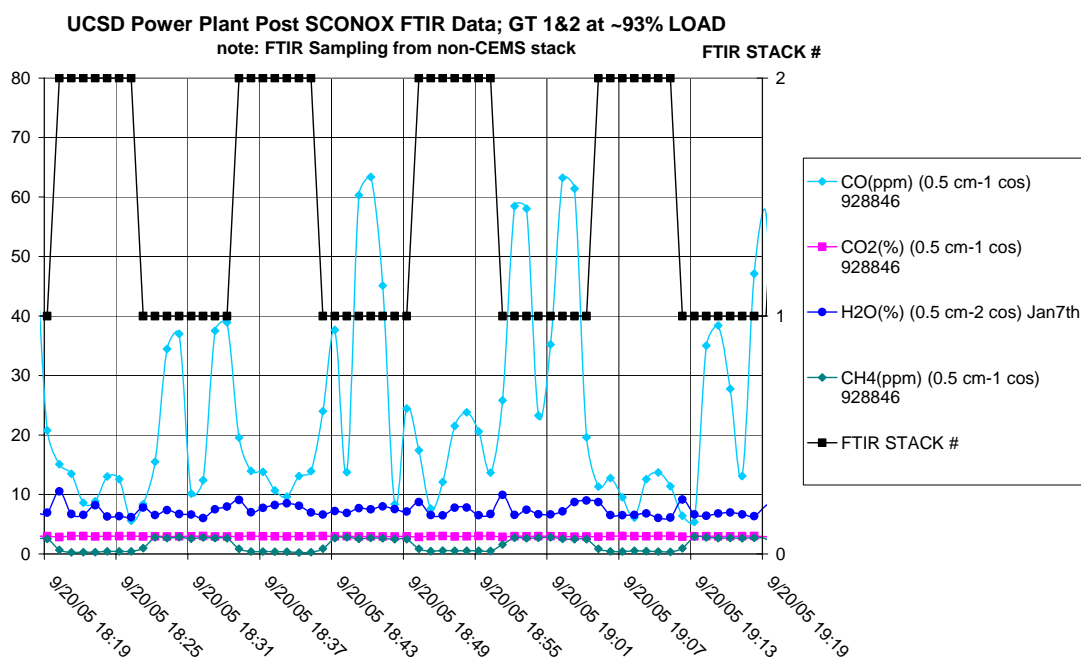
Figure 5.7: FTIR 1-hour time period from 9/20/05 showing CO, CO$_2$, H$_2$O, and CH$_4$ along with FTIR stack number; gas turbines operating close to 93% load (refer to Table 5.2 for FTIR species units)

Figures 5.2 through 5.7 focused on H_2O, CO_2, CO, and CH_4 since they could also be measured using the TDL system. With the gas turbines operating between 85 to 94 percent load, the FTIR detected H_2O content in the 5 to 10% range and CO_2 content around 2.9 to 3.1%. CO ranged from 0 to 90 ppm (0 to 20 ppm for GT2) and CH_4 was less than 5 ppm (less than 1 ppm for GT2).

5.3 TDL Field Data

TDL field data was collected from the UCSD power plant on two occasions. The first attempt was made along with the FTIR data collection in September 2005. The logged TDL data was not valid since the normalized H_2O, CO_2, CO, and CH_4 peak amplitude data was calculated incorrectly inside the Labview VI (program). An overview of the Round 1 data is shown in Figure 5.8.
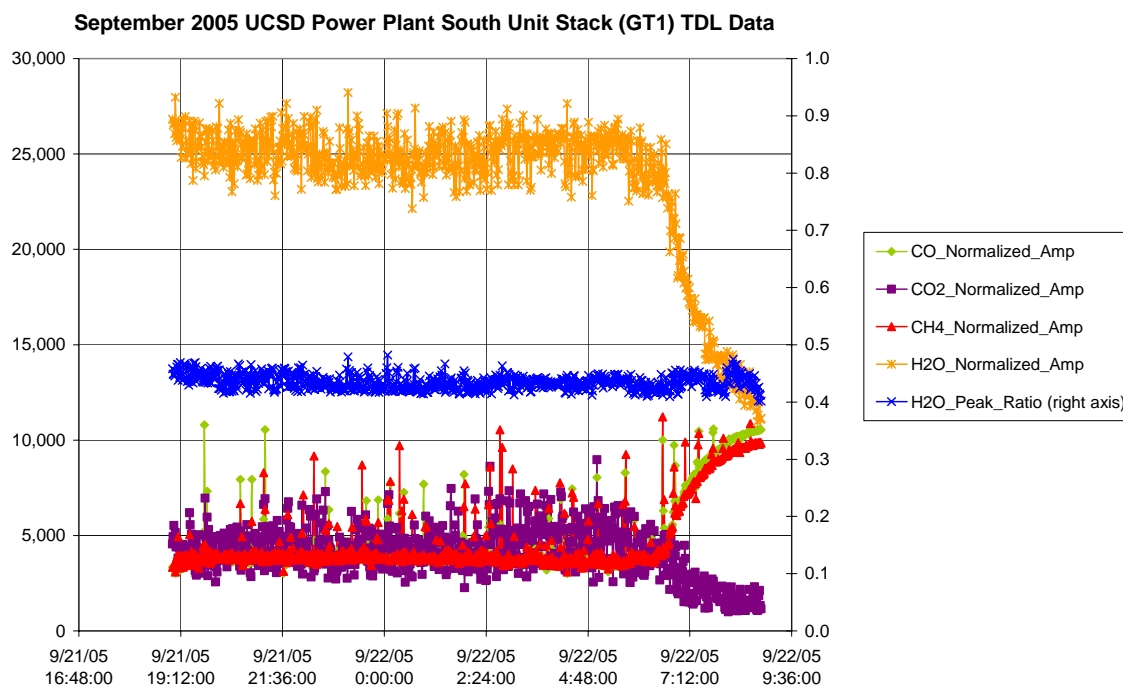
Figure 5.8: The first 14 hours of TDL field data collected in September 2005

All of the normalized peak amplitudes shown in Figure 5.8 should be less than 1. Despite the poor results, we did prove that beam-steering and exhaust stack window condensation and fouling were not issues. We also learned that we were not able to detect the small concentrations of CO and CH_4 (less than 100 ppm) present in the exhaust. This experience prepared us for the second round of testing in April 2006 where we re-wired the TDL box optimized to take H_2O and CO_2 data. The Labview VI used to capture the data was also corrected and upgraded. This data is the basis for this thesis and is presented in this chapter.

In April 2006, the TDL system was set up on the existing south unit stack window fixtures. Six parameters were recorded by the TDL Labview program: Time (sec), Ratio, 1st H_2O normalized peak, CO_2 normalized peak, 1st H_2O peak, and CO_2 peak amplitude. Snapshot data was captured every 0.5 seconds starting at 10:59 on 4/2/06 and ending at 15:00 on 4/10/06. The gas turbine ran continuously over this time period.

Over eight days worth of ½-second TDL data proved to be a data reduction challenge since 1,422,123 rows of data were captured. Since Excel can only handle 65,536 rows of data, Igor Pro version 3.1.4.0 was used to reduce and plot the data. In order to calculate and display meaningful temperature, H_2O, and CO_2 concentration data, the following steps were taken. First, the data was filtered to remove outliers caused by noise in the laser. Second, the data was decimated (an Igor Pro function, explained below) to average the filtered ½ second data into 1-minute intervals. Third, in order to compare the TDL data to the FTIR data based on gas turbine percent load, hourly data was extracted. Table 5.3 summarizes the data from its raw to filtered and then decimated state. The outliers in the raw data set make up a small percentage of the overall data for

all of the parameters except for the normalized CO_2 peak amplitude as shown in the hard filter section of the table (calculated using statistical software MiniTab). Only 0.67% of the H_2O peak ratio data and 1.12% of the normalized H_2O peak amplitude was outside the hard filter bounds compared to 54% for the normalized CO_2 peak amplitude data.

The first step in the data reduction and filtering was done using an Igor procedure written by Gharavi. The code checks if each data point is greater than the upper bound or less than the lower bound. If either case is true, a user-defined in-place average replaces the data point. The bounds and in-place averages used are listed in Table 5.3. The second step in the data reduction was completed using an Igor function called Decimate that simply averages a user-defined number of data points into one. A decimation factor of 120 was used in order to turn the filtered ½ second data into 1-minute averages. A third data reduction step was taken in order to compare the FTIR and TDL data as a function of gas turbine percent load. Since the gas turbine data is hourly, the TDL data was reduced such that data each hour was retained. This was done with code in Igor.

Table 5.3: Table of TDL April 2006 field data from GT1 with data reduction summary

		Ratio	First H2O Norm	CO2_Norm	First H2O Ampl	CO2 Ampl
Raw Data	# of Datapoints	1,422,123	1,422,123	1,422,123	1,422,123	1,422,123
	Minimum	-2.72E+01	-4.51E+00	-1.72E+06	-3.15E+00	7.31E+06
	Maximum	5.03E+01	1.82E+01	6.03E+06	6.12E+00	5.68E+00
	Average	6.50E-01	6.61E-01	6.40E+00	4.94E-01	2.71E-02
	Standard Deviation	1.05E-01	9.07E-02	7.79E+03	6.50E-02	5.44E-02
	% Standard Deviation	16.1%	13.7%	121725.0%	13.2%	200.8%
Hard Filter	Lower Bound	0.60	0.60	0.10	0.40	0.02
	Upper Bound	0.70	0.75	0.33	0.56	0.07
	# of Datapoints	1,412,544	1,406,178	646,802	1,411,686	1,410,294
	% Reduction	0.67%	1.12%	54.52%	0.73%	0.83%
IGOR Filter	Lower Bound	0.58	0.58	0.00		
	Upper Bound	0.72	0.86	1.00		
	In Place Average	0.65	0.66	0.18		
	# of Datapoints	1,422,123	1,422,123	1,422,123		
	Minimum	0.58	0.58	0.01		
	Maximum	0.72	0.86	1.00		
	Average	0.65	0.66	0.19		
	Standard Deviation	1.55E-02	2.53E-02	3.46E-02		
	% Standard Deviation	2.4%	3.8%	17.9%		
IGOR Decimation	Decimation Factor	120	120	120		
	# of Datapoints	11,851	11,851	11,851		
	Minimum	0.63	0.62	0.16		
	Maximum	0.66	0.71	0.27		
	Average	0.65	0.66	0.19		
	Standard Deviation	5.04E-03	1.74E-02	1.79E-02		
	% Standard Deviation	0.8%	2.6%	9.2%		

The raw H_2O peak ratio data from April 2006 is shown in Figure 5.9. The noise is apparent but random. The cause is believed to be changes in laser power and fiber optic cable movement. By zooming in to a 1-hour time period it is clear that the majority of data falls into a much tighter band between 0.58 and 0.72 as shown in Figure 5.10.
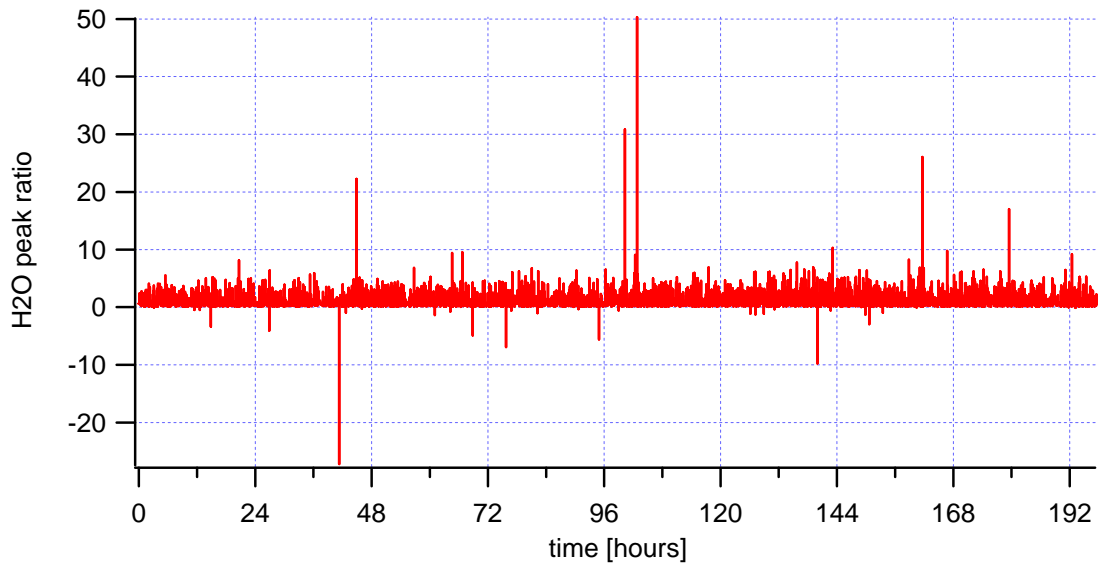
Figure 5.9: April 2006 GT1 TDL H_2O peak ratio <u>raw</u> data (entire data set)
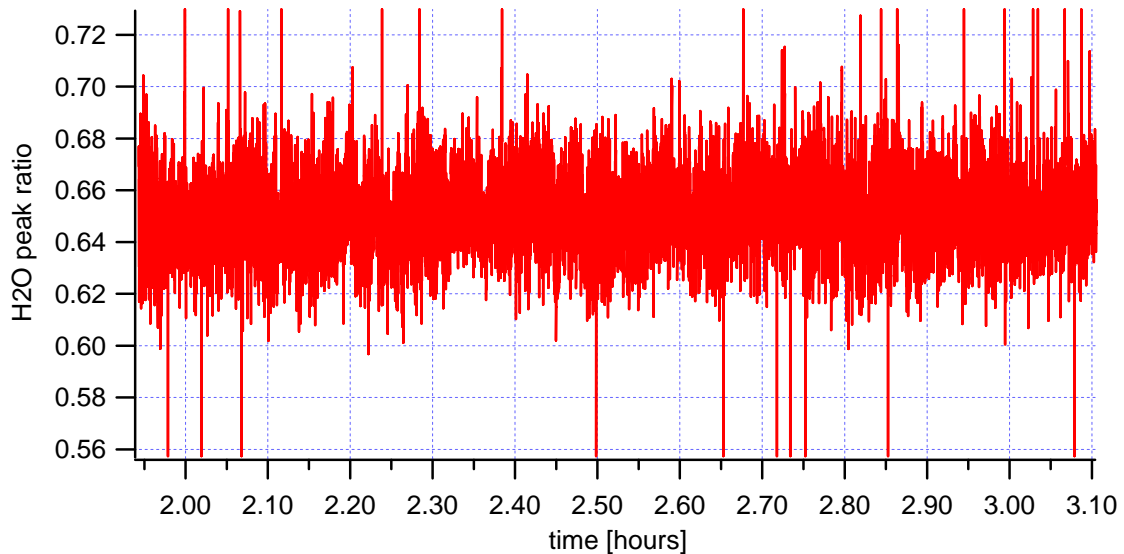
Figure 5.10: April 2006 GT1 TDL H_2O peak ratio <u>raw</u> data (early 1-hour time period)

The filtering and then decimation of the raw H_2O peak ratio data shows a clearer picture of the trend over the 196-hour test. These results are shown in Figures 5.11 and 5.12 below.
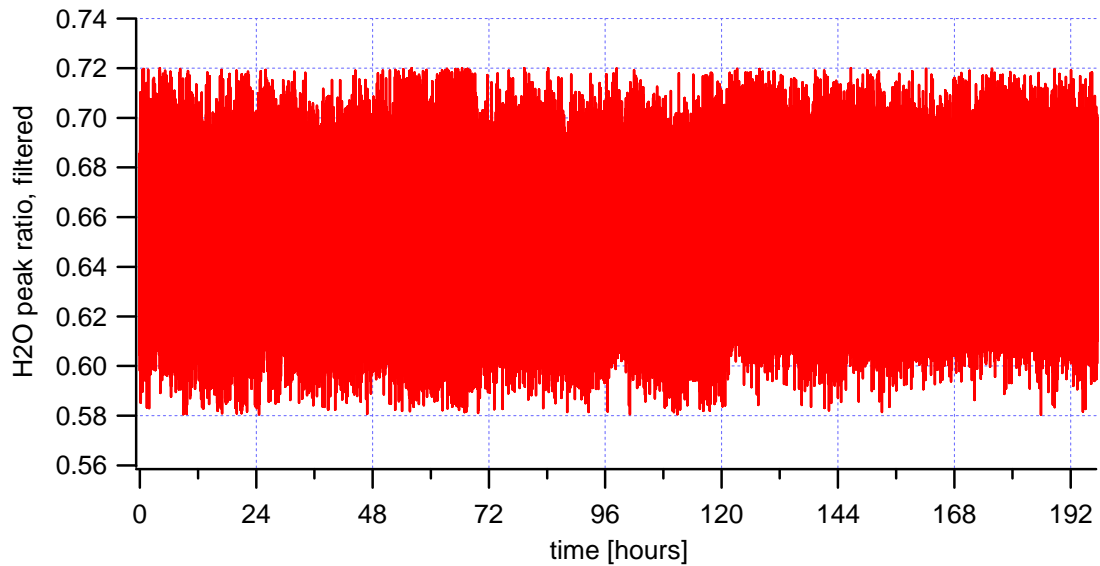
Figure 5.11: April 2006 GT1 TDL H_2O peak ratio <u>filtered</u> data (entire data set)
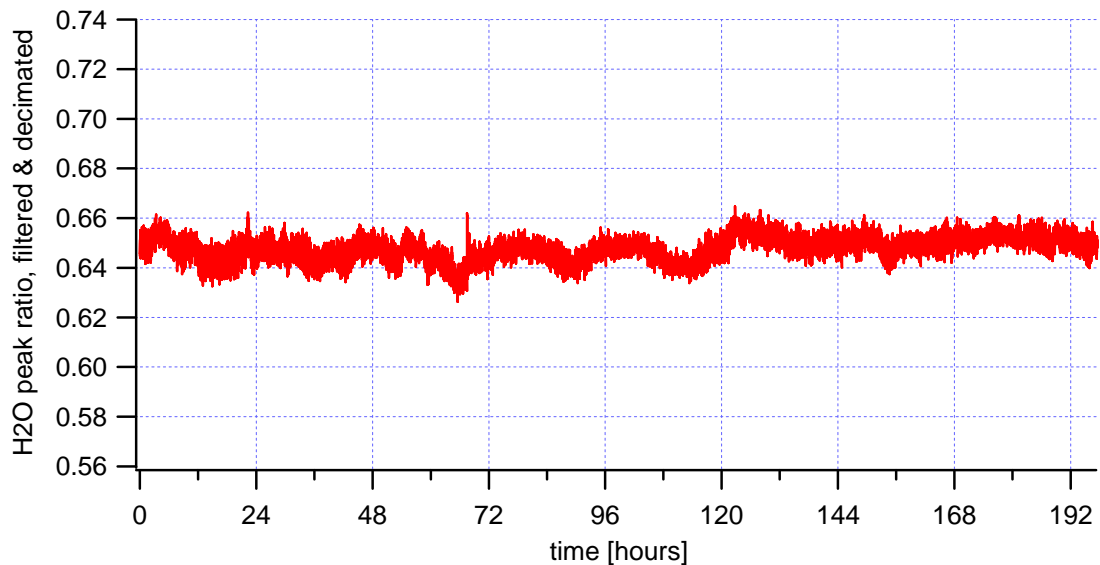
Figure 5.12: April 2006 GT1 TDL H_2O peak ratio <u>filtered & decimated (1-minute average)</u> data (entire data set)

The next step was to determine if the changes in TDL H_2O peak ratio correspond to actual temperature changes in the exhaust flow. To do this, H_2O peak ratio was plotted along with the gas turbine (GT1) percent load in Figure 5.13. It does appear that the H_2O peak ratio changes correspond to changes in gas turbine load.
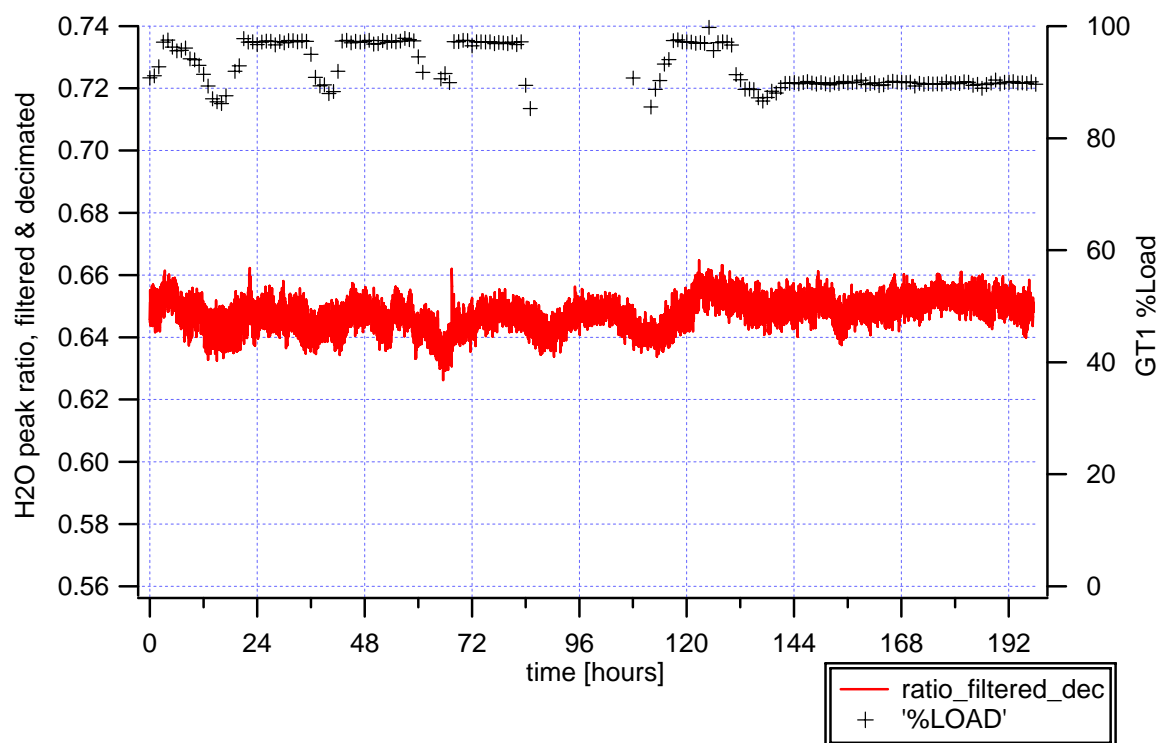
Figure 5.13: April 2006 GT1 TDL H_2O peak ratio filtered & decimated (1-minute average) data (entire data set) along with GT1 hourly percent load data

Following the methodology outlined in Chapter Four, the filtered and decimated H_2O peak ratio data was converted to temperature in Kelvin as shown in Figure 5.14. The temperature ranges between 424 and 440 K with an average of 433 K.
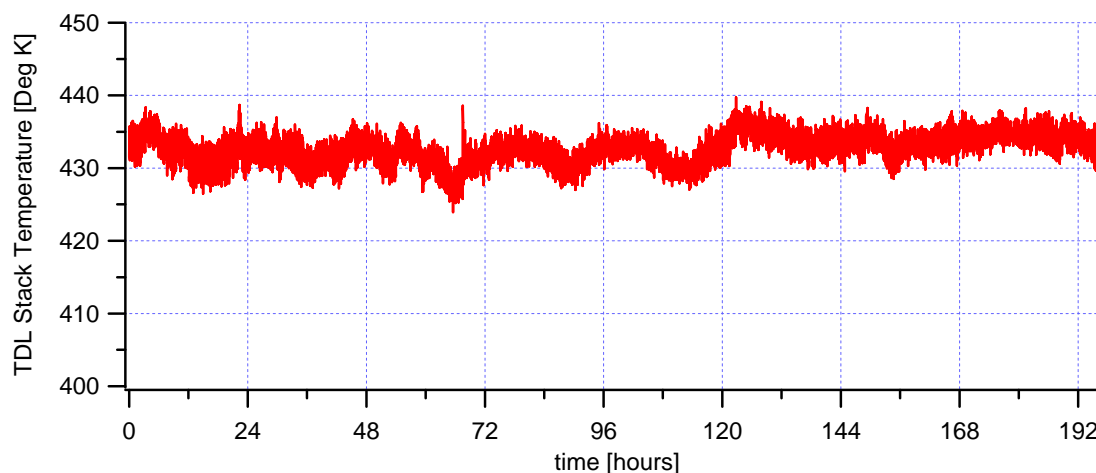
Figure 5.14: April 2006 GT1 TDL calculated stack exhaust temperature data (entire data set)

The TDL Labview computer did not have a TC input card so exhaust temperature data was not collected for the duration of the test. Future studies should collect this data. A stack exhaust temperature survey at the TDL measurement plane was completed the day before testing began however. The radial survey was done using a sealed Type K thermocouple connected to a Fluke TC reader. The results are shown in Figure 5.15.
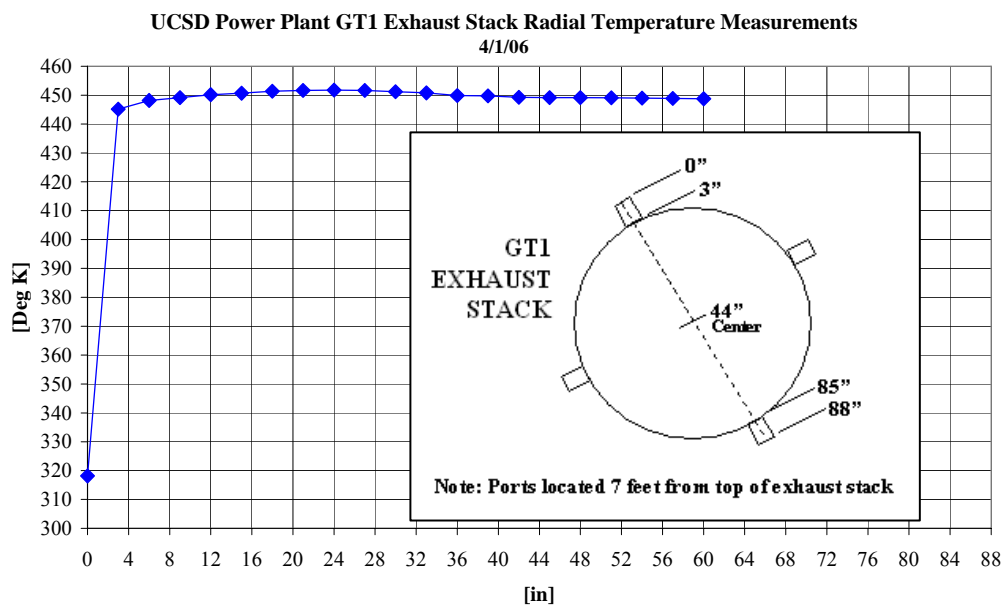
Figure 5.15: GT1 exhaust stack radial temperature measurement results

Aside from the boundary layer measurement closest to the wall, the temperature profile was found to be flat with an average temperature of 450 K and a range of 7 K. These results are around 17 K higher than the TDL calculated exhaust temperature.

The TDL exhaust stack temperature can also be compared to the measured gas turbine exhaust temperature. Three N-Type TC's measure the exhaust temperature in the turbine exhaust collector downstream of the final turbine disk. This is referred to as the T7 plane. The exhaust flow then travels through the evaporator, ScoNOx system, and economizer before reaching the TDL measurement plane, which explains the roughly 330 K drop in temperature between the two points as shown in Figure 5.16.
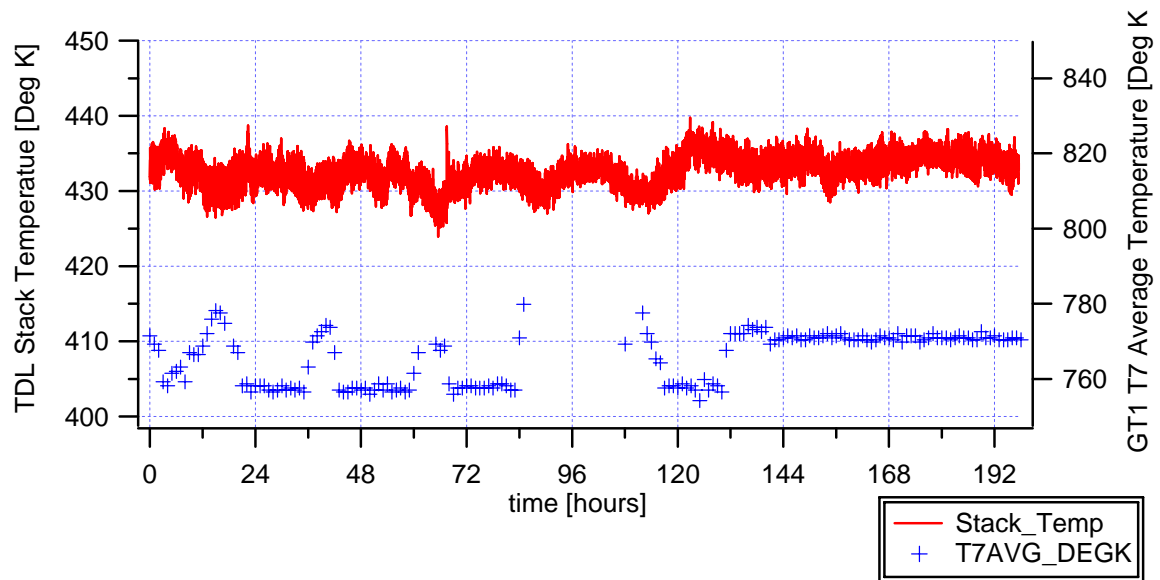
Figure 5.16: TDL exhaust stack and GT1 T7 temperature data over the April 2006 testing

The trends between the TDL and gas turbine exhaust temperatures seem to match but it is unclear why they are in opposite directions. When there is an increase in gas turbine measured T7 there is a corresponding decrease in TDL calculated exhaust temperature. Perhaps the heat recovery and/or ScoNOx systems account for this observation.

From the gas turbine perspective the T7 exhaust temperature decreases with load between 50 to 100% load, in which the turbine operates in dry lean pre-mixed low emissions mode (known as SoLoNOx by Solar Turbines Inc.). In SoLoNOx mode, electronic valves control the fuel and inlet guide vanes on the turbine axial compressor control the airflow to meet a desired third stage rotor inlet temperature (T5) in order to meet power and low emissions requirements. The T5 temperature remains constant while in SoLoNOx mode. An idealized T-s diagram shown in Figure 5.17 highlights why this scenario produces higher exhaust temperatures at part-load conditions. Figure 5.18 depicts this relationship by plotting measured T7 average exhaust temperature as a function of gas turbine percent load.
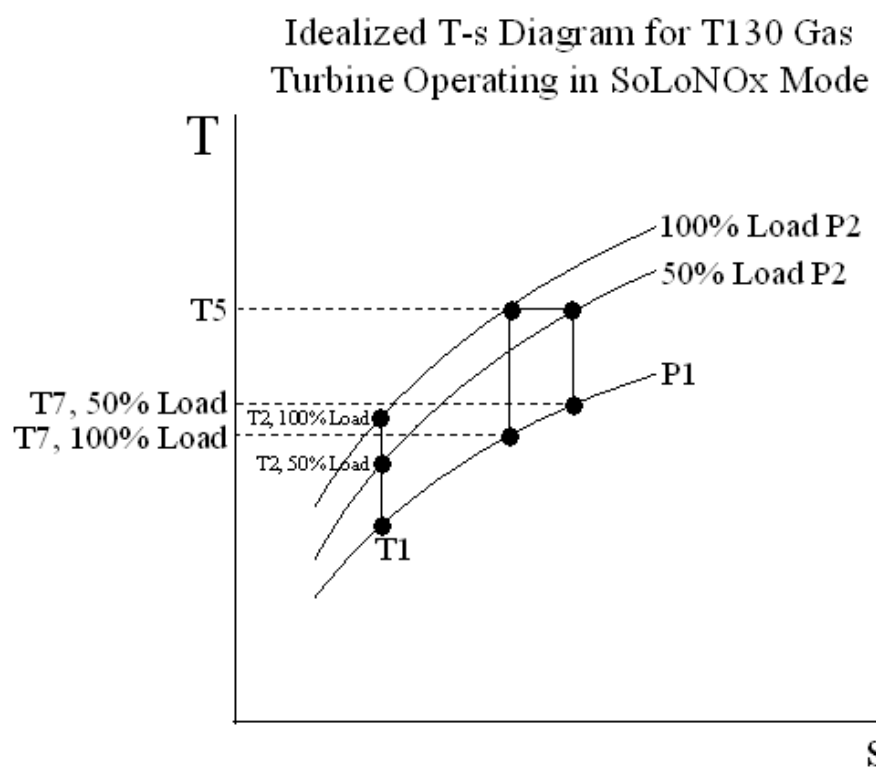
Figure 5.17: Idealized T-s diagram for a Titan 130 gas turbine operating in SoLoNOx mode
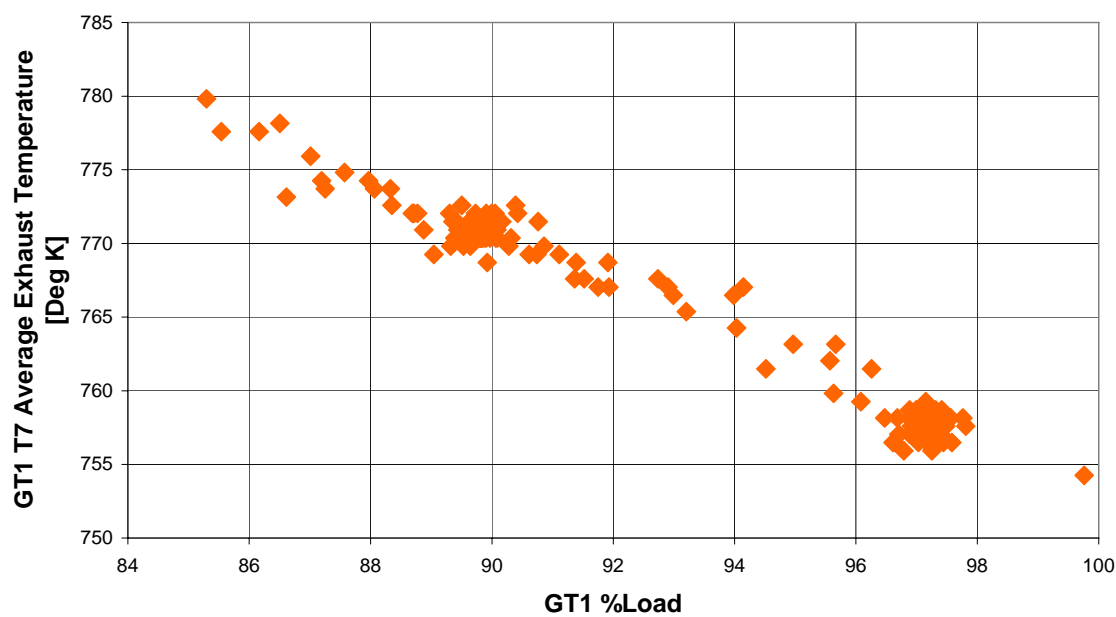
Figure 5.18: April 2006 testing GT1 T7 average temperature vs percent load (hourly data)

In Figure 5.19, the TDL exhaust stack temperature is plotted along with the gas turbine percent load. Opposite of the gas turbine exhaust temperature (T7) trend versus load, the TDL exhaust stack temperatures are highest at higher gas turbine loads.
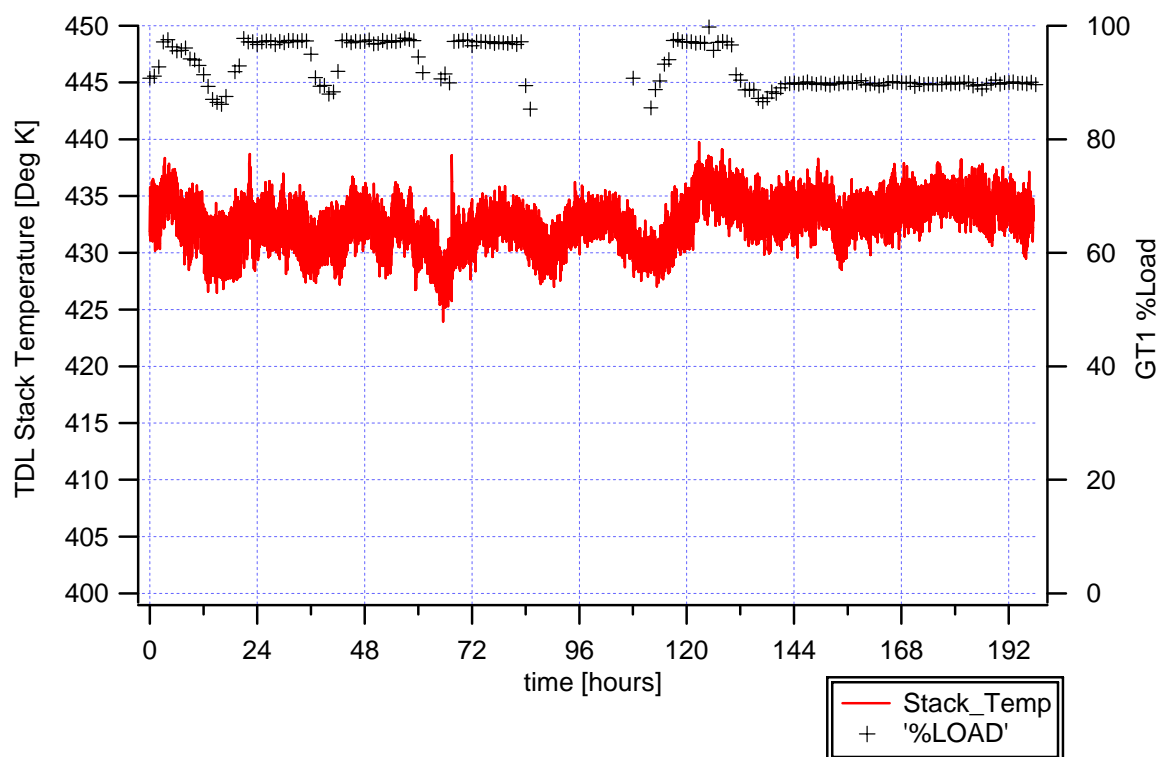
Figure 5.19: TDL exhaust stack temperature and GT1 percent load data over the April 2006 testing

H_2O and CO_2 content in the exhaust flow were also measured by the TDL system. Like the H_2O peak ratio data the same data reduction steps were taken. As defined in Chapter 4, H_2O content is calculated using the H_2O normalized peak amplitude TDL data. The raw peak amplitude and normalized peak amplitude H_2O data is shown in Figure 5.20 and 5.21. The filtering removed the noisy ½ second H_2O normalized peak amplitude data while the decimation allowed for a tighter trend to appear. These plots are shown in Figures 5.22 and 5.23. The filtered and decimated H_2O normalized peak

amplitude data was then used to calculate H_2O mole fraction over the test period as shown in Figure 5.24.
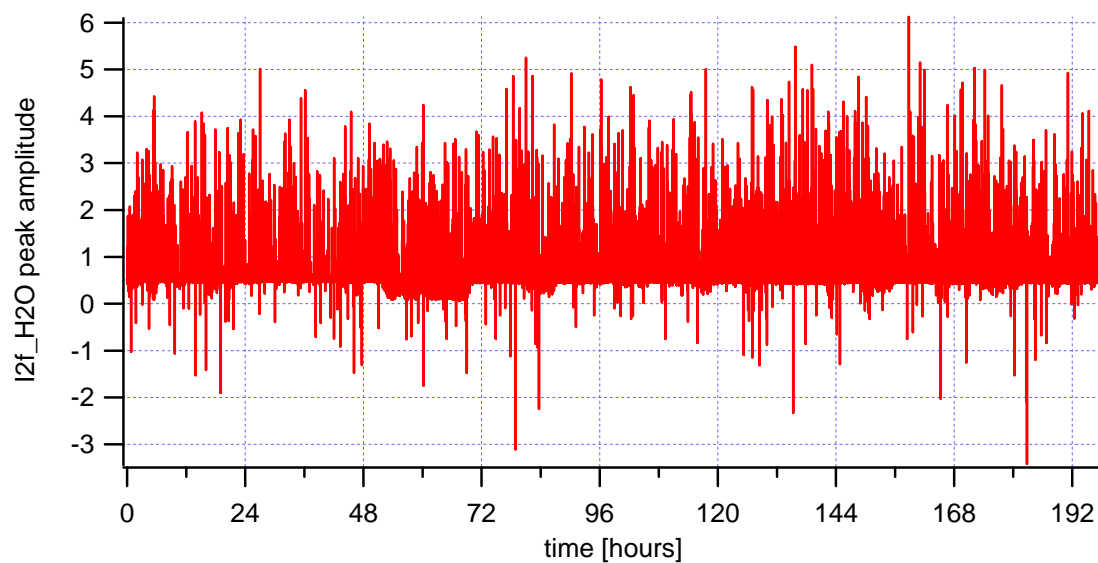
Figure 5.20: TDL raw H_2O peak amplitude data over the entire April 2006 test period
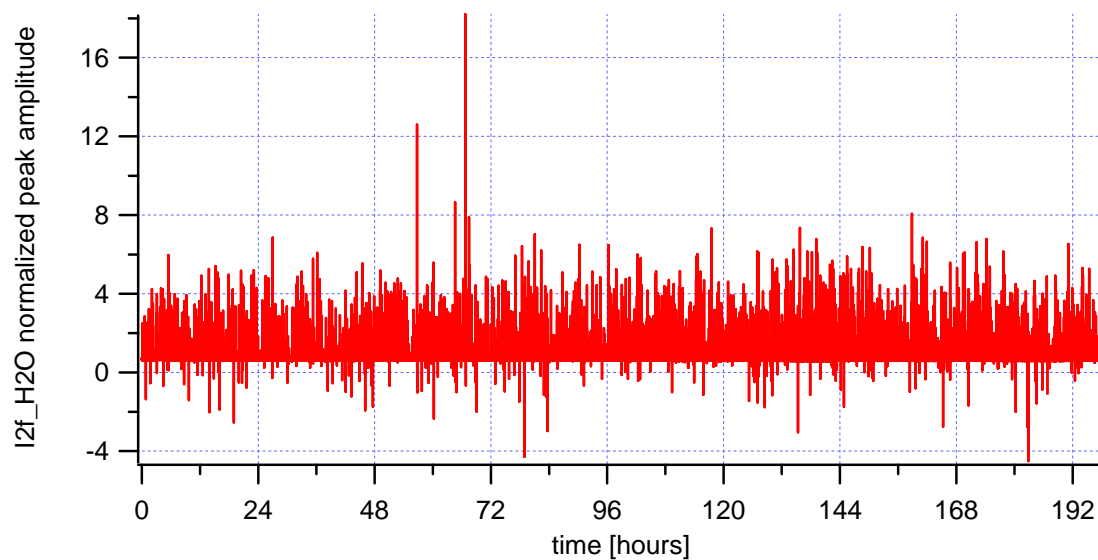
Figure 5.21: TDL raw H_2O normalized peak amplitude data over the entire April 2006 test period
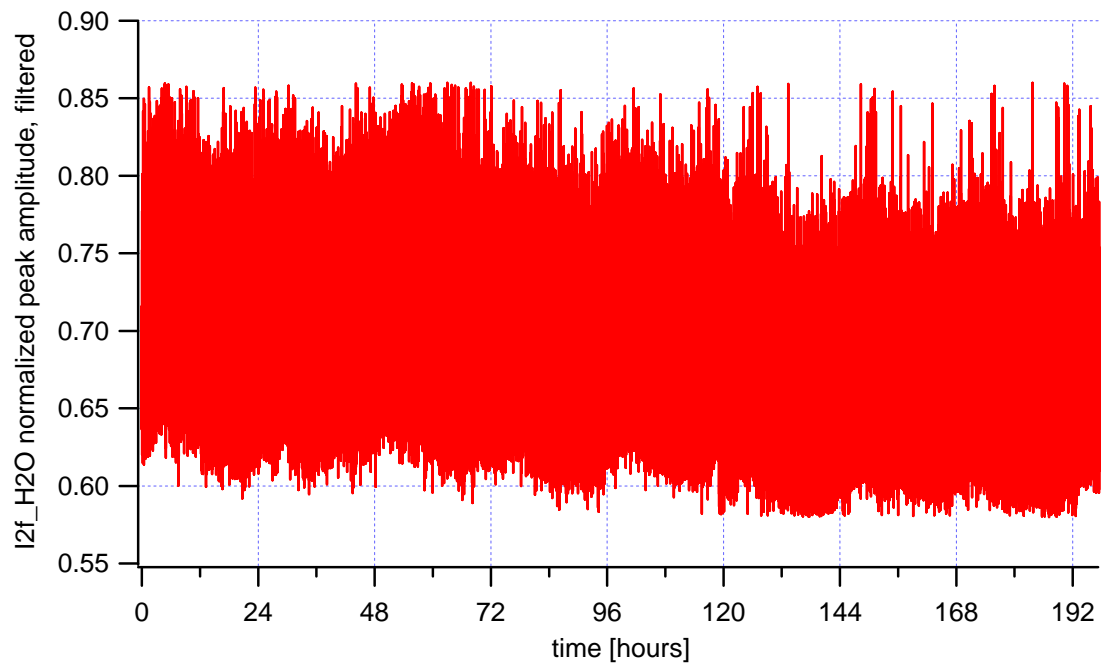
Figure 5.22: TDL H_2O normalized peak amplitude <u>filtered</u> data over the entire April 2006 test period
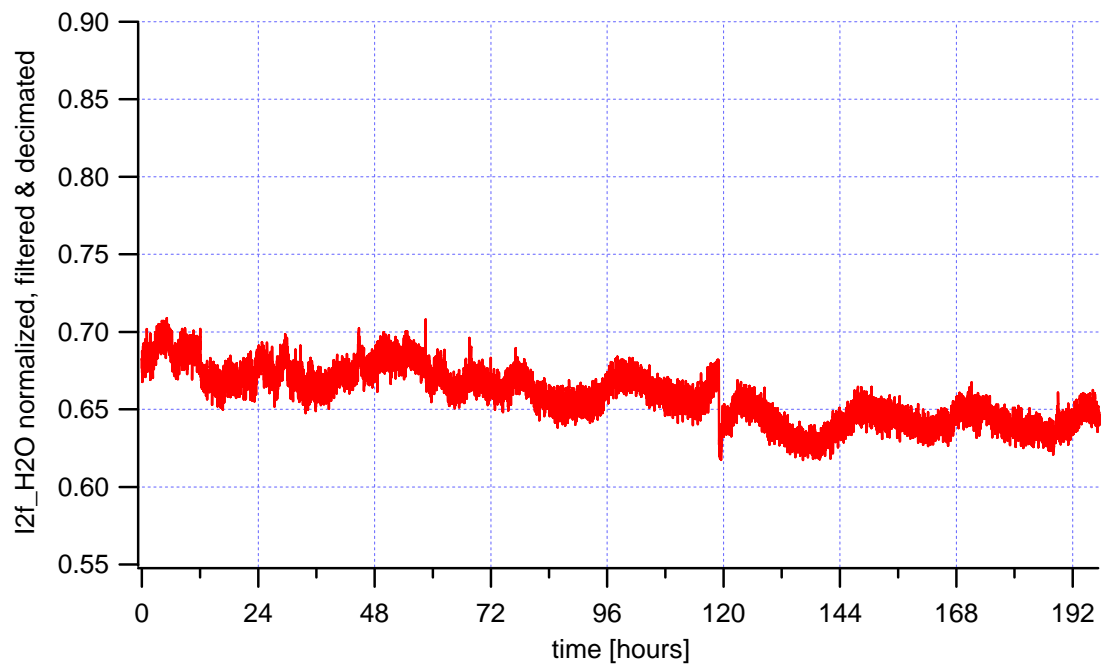
Figure 5.23: TDL H_2O normalized peak amplitude <u>filtered & decimated (1-minute average)</u> data over the entire April 2006 test period
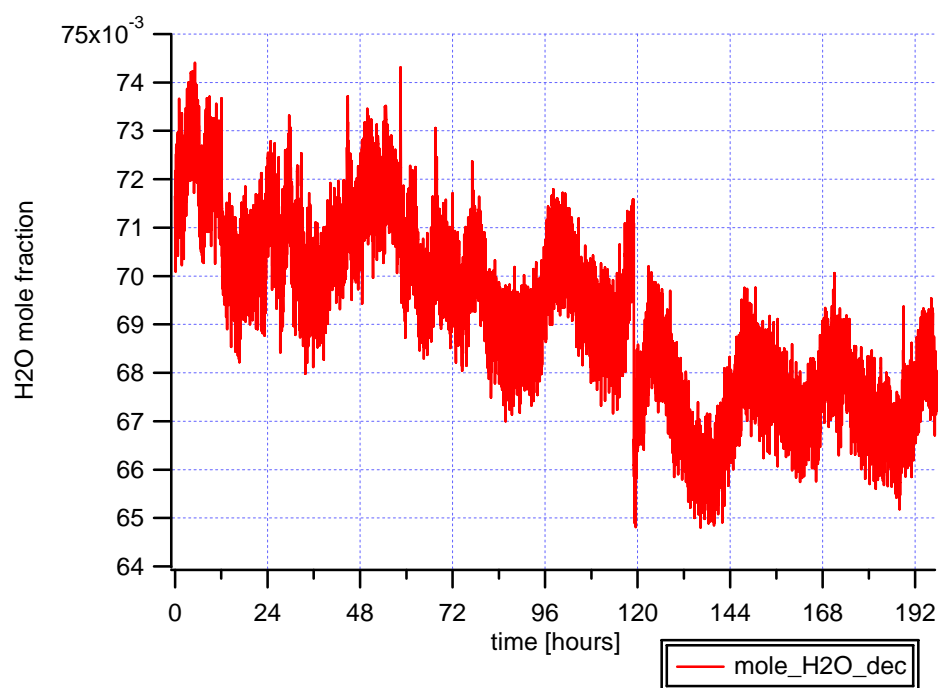
Figure 5.24: TDL H_2O mole fraction based on the <u>filtered & decimated (1-minute average)</u> H_2O normalized peak data over the entire April 2006 test period
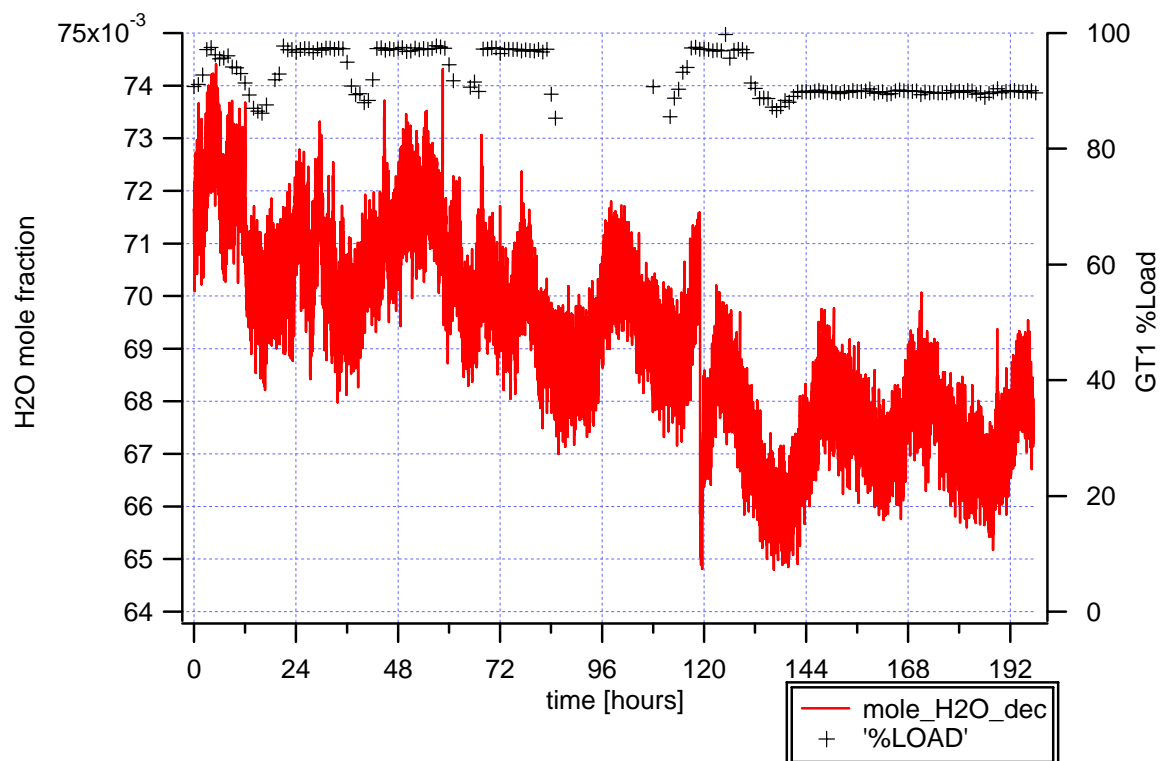
Figure 5.25: TDL H_2O mole fraction based on the <u>filtered & decimated (1-minute average)</u> H2O normalized peak data along with GT1 percent load over the entire April 2006 test period

The filtered and decimated H_2O content varied between 6.5 and 7.4 percent over the April 2006 test period. The downward trend can be explained by the shift in content just before the 120-hour mark. The H_2O content appears to be cyclic, changing around 0.5% over each 24-hour period. Adding GT1 percent load over the test period is shown in Figure 5.25. This generally shows that H_2O content is highest at full load.

The CO_2 content over the test period was not as stable. This can be explained by the fact that the CO_2 peak signal is not as strong as H_2O. As discussed in Chapter 4, CO_2 content is calculated using the CO_2 normalized peak amplitude TDL data. The raw peak amplitude and normalized peak amplitude CO_2 data is shown in Figures 5.26 through 5.29. The filtering removed the noisy ½ second CO_2 normalized peak amplitude data while the decimation allowed for a tighter trend to appear. The normalized peak CO_2 data is much cleaner up to the 12-hour and after the 118-hour points. These plots are shown in Figures 5.30 and 5.31. The filtered and decimated CO_2 normalized peak amplitude data is then used to calculate CO_2 mole fraction over the test period as shown in Figures 5.32 and 5.33.
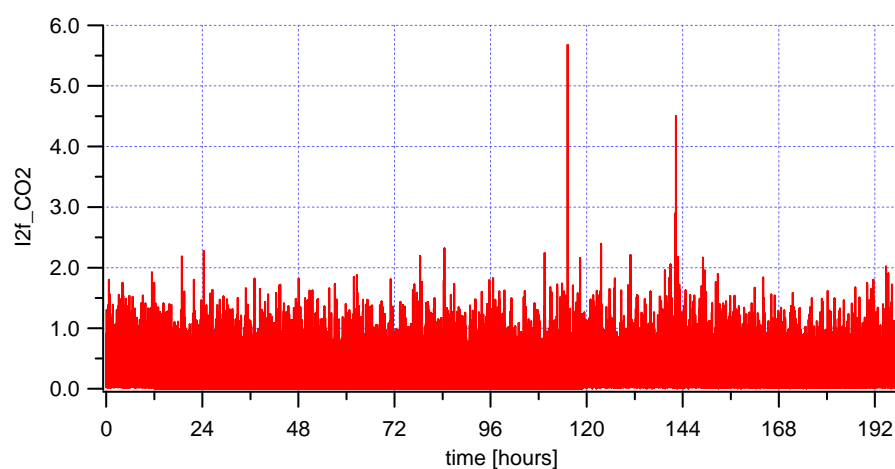
Figure 5.26: TDL raw CO_2 peak amplitude data over the entire April 2006 test period

Figure 5.27: TDL raw normalized CO_2 peak amplitude data over the entire April 2006 test period
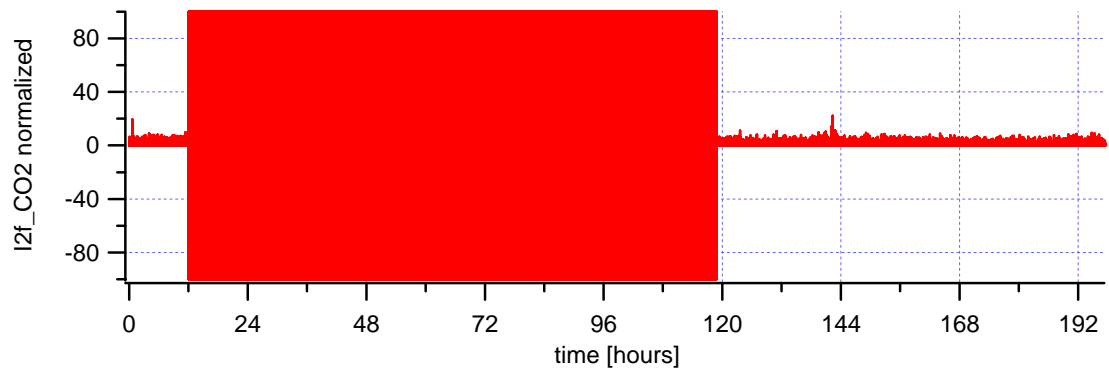
Figure 5.28: TDL raw normalized CO_2 peak amplitude data over the entire April 2006 test period showing the noisy data between 12 and 118 hours
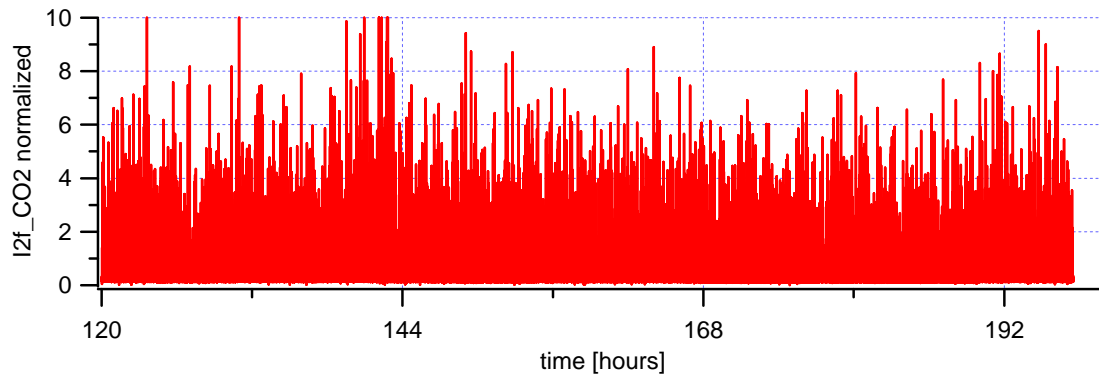
**Figure 5.29:** TDL raw normalized CO_2 peak amplitude data after 120 hours
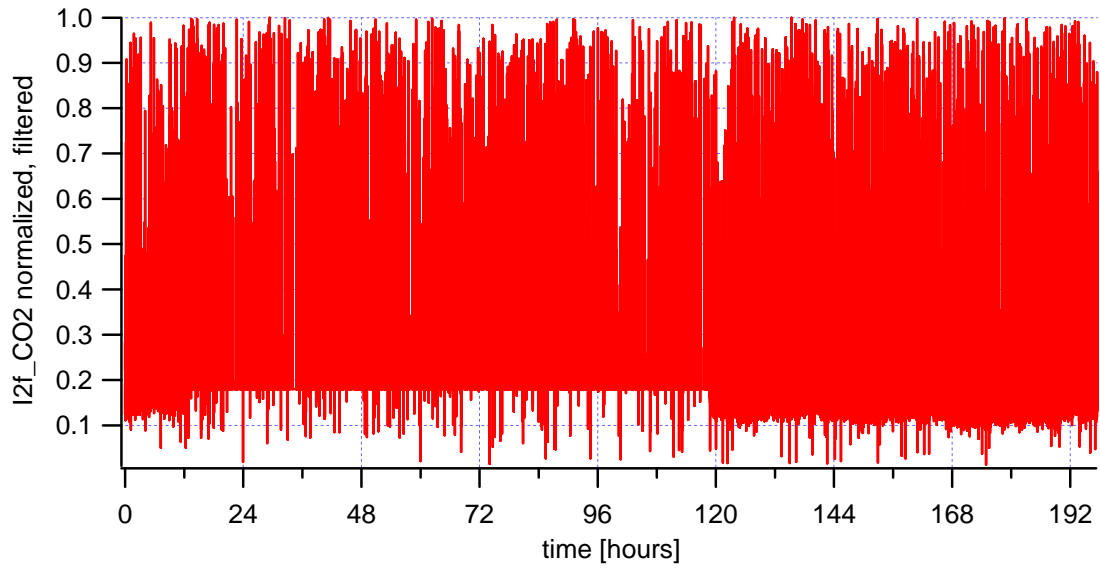
Figure 5.30: TDL normalized CO_2 peak amplitude <u>filtered</u> data over the entire April 2006 test period
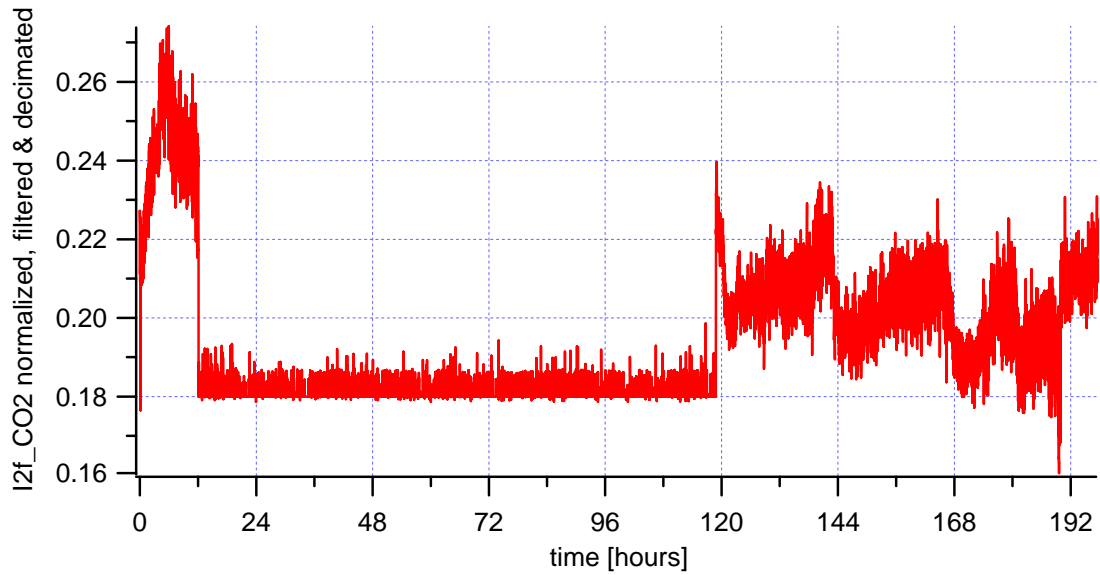
Figure 5.31: TDL normalized CO_2 peak amplitude <u>filtered & decimated (1-minute average)</u> data over the entire April 2006 test period
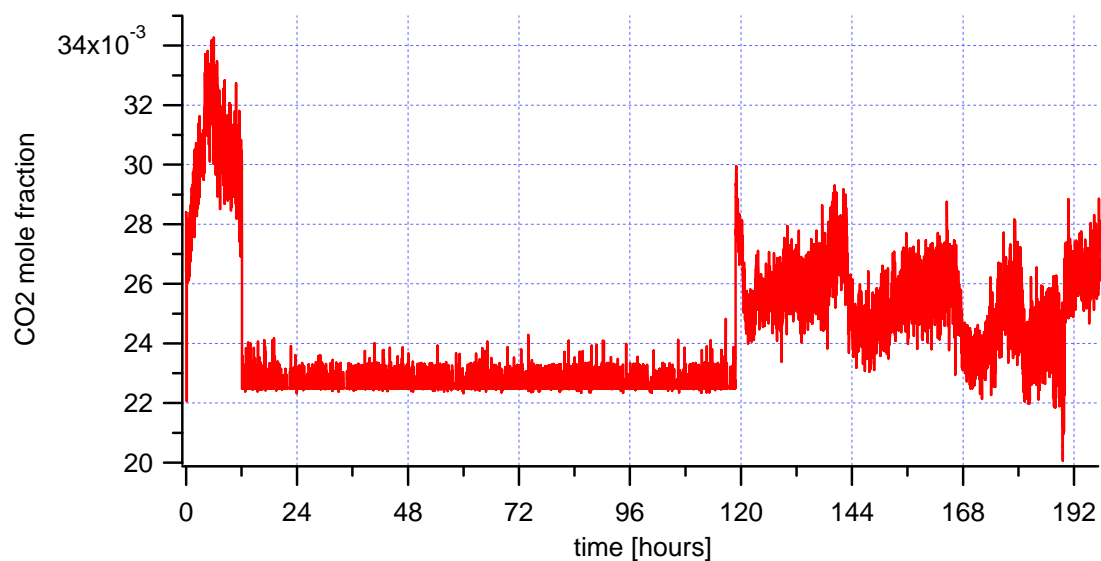
Figure 5.32: TDL CO_2 mole fraction based on the <u>filtered & decimated (1-minute average)</u> CO_2 normalized peak data over the entire April 2006 test period
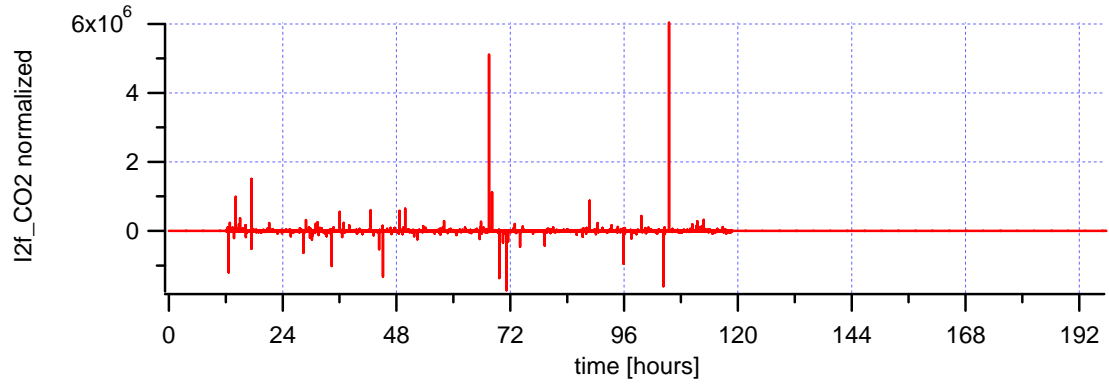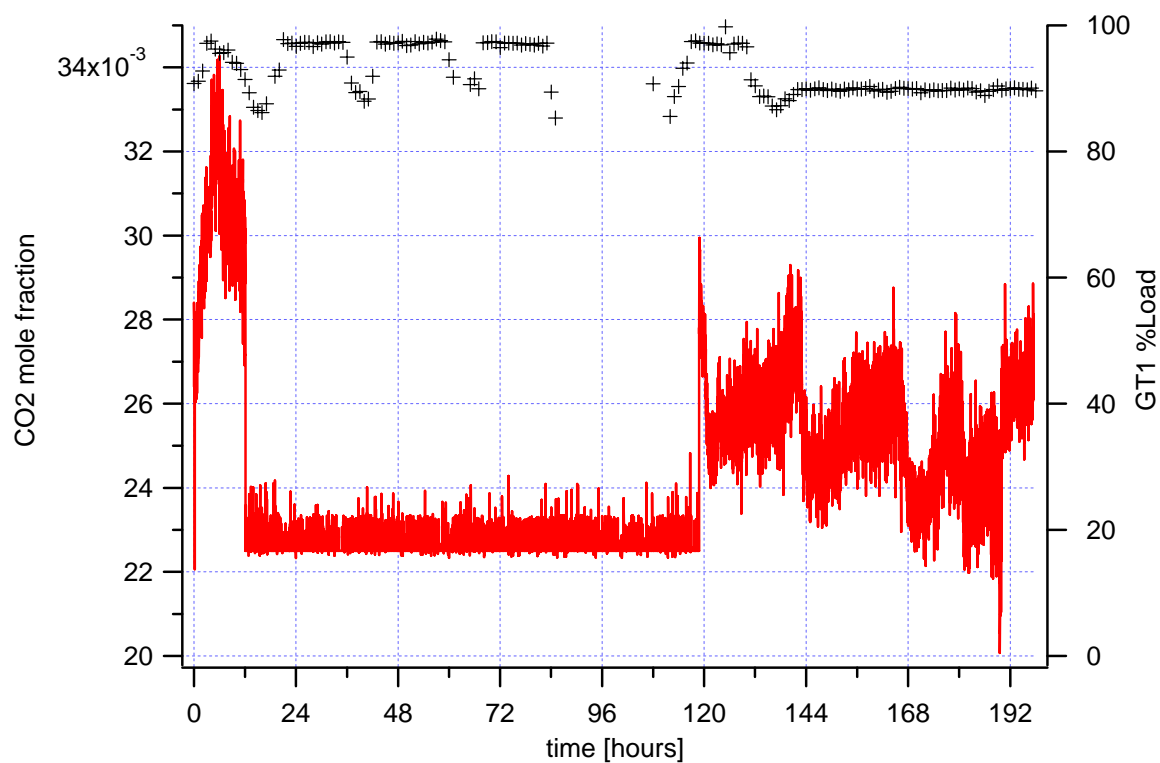

Figure 5.33: TDL CO_2 mole fraction based on the <u>filtered & decimated (1-minute average)</u> CO_2 normalized peak data along with GT1 percent load data over the entire April 2006 test period

The CO_2 content varied between 2.0 and 3.4%. After the 120-hour mark the results were more reasonable and appeared to be cyclic like H_2O. The data between 12 and 120 hours should be discounted as something was TDL setup was amiss. A strong relationship between CO_2 and GT1 percent load did not exist.

5.4 FTIR & TDL Field Data Comparison

GT1 percent load can be used to compare the TDL results from the April 2006 testing and the FTIR data from September 2005. To do this, the data needed to be matched up in time to the hourly gas turbine data. This was done manually for the minute post-ScoNOx FTIR data. The decimated 1-minute average TDL data was resolved into hourly snapshot data using code written in Igor. Once the hourly FTIR and TDL data was linked to the gas turbine data, the following two plots of H_2O and CO_2 content versus percent load were generated (Figures 5.34 & 5.35).
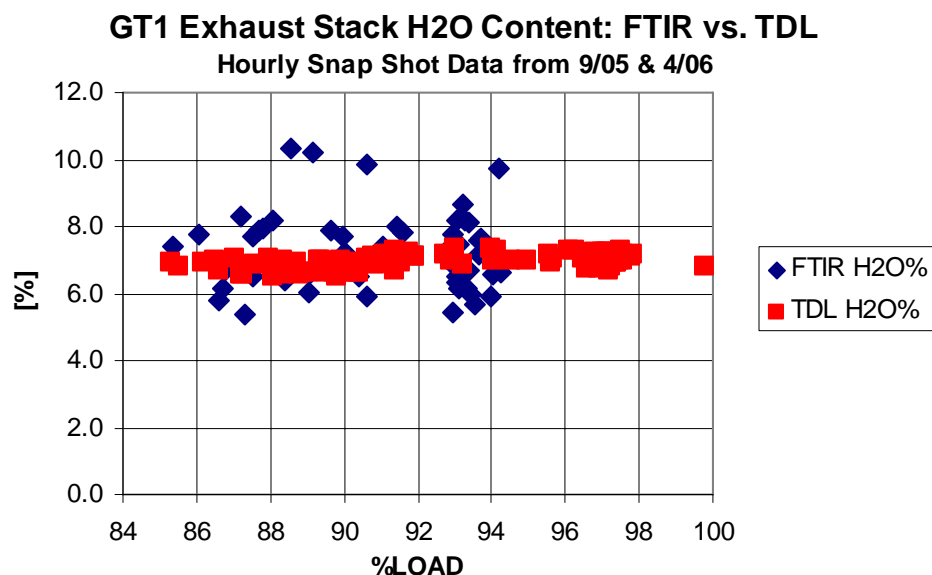
Figure 5.34: GT1 exhaust stack H_2O content as a function of percent load for the 9/05 FTIR and 4/06 TDL data

GT1 Exhaust Stack CO2 Content: FTIR vs. TDL

Hourly Snap Shot Data from 9/05 & 4/06
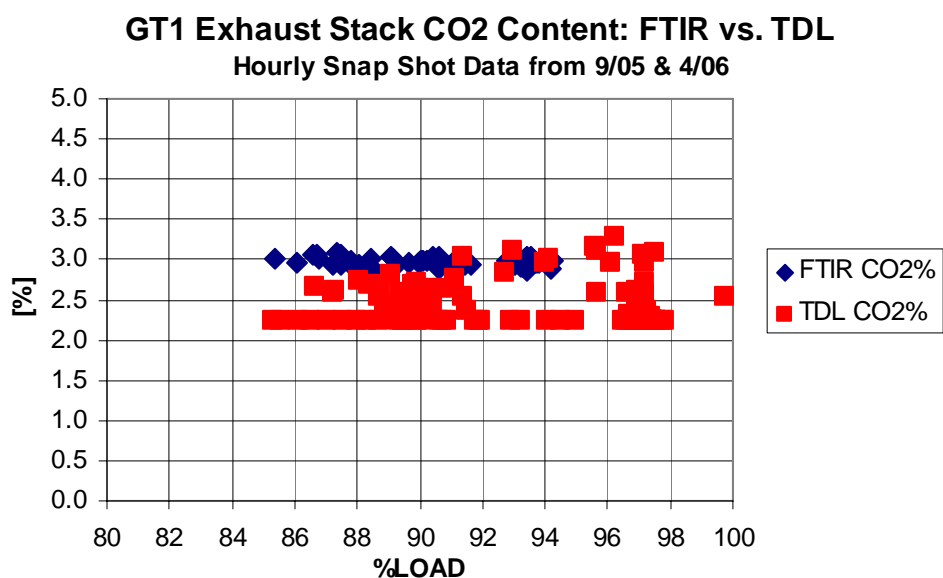
Figure 5.35: GT1 exhaust stack CO_2 content as a function of percent load for the 9/05 FTIR and 4/06 TDL data

The TDL H_2O content data was much tighter than that from the FTIR with only a 1% spread instead of 5%. The opposite is true for CO_2 where the FTIR showed a 0.2% spread while the TDL data exhibited over 1%. The latter may be explained by the fact that the mid-IR CO_2 peak measured by the FTIR is extremely strong, while as mentioned above, the TDL is measuring a relatively weak CO_2 absorption line in the near-IR.

5.5 Error Analysis

The TDLAS results presented in this research had the luxury of being benchmarked against secondary sources. Field TDL WMS concentration data was compared to a commercially available FTIR system while field gas turbine stack exhaust temperature measurements were taken at the same plane as the TDL line of sight. TDL-specific uncertainties will also be covered in this section.

Comparison of the average TDL WMS and TC gas turbine exhaust temperatures from Figures 5.14 and 5.15 showed that the TDL WMS system measured temperatures around 3.7% lower (433 K versus 450 K). The TDL temperature measurement corresponded to a path-averaged temperature that included colder boundary layer effects. The TDL versus TC exhaust temperature difference was also within the laboratory calculated TDL temperature uncertainty of $\pm$ 24.9 ºC (Gharavi 2004).

Since the field FTIR and TDL concentration data were taken on different occasions, both sets of data were compared as a function of gas turbine load as shown in Figures 5.34 and 5.35. From Figure 5.34, it is clear that the TDL H_2O measurements had much less variation compared to the FTIR data. While both averages were around 7% concentration, the TDL data range (minimum to maximum for the data set) was 0.8% percent concentration compared to 4.9% for the FTIR. The H_2O TDL standard deviation was 0.19% compared to 1.10% for the FTIR data. This can be explained by the relatively strong H_2O TDL WMS signal and the fact that water was most likely condensing somewhere inside the long heated FTIR feed lines. As shown in Figure 5.35, the TDL CO_2 data fluctuated more than the FTIR data, with a range of 1% concentration compared to a range of 0.2% for the FTIR data. The TDL CO_2 standard deviation was also worse at

0.23% compared to 0.05% for the FTIR. The TDL CO_2 concentration average was around 2.4% while the FTIR average concentration was a 3.0%. This difference is attributed to the weak TDL WMS CO_2 signal.

The results are summarized best by comparing the ratios of the standard deviation to the mean for the TDL and FTIR measurements.
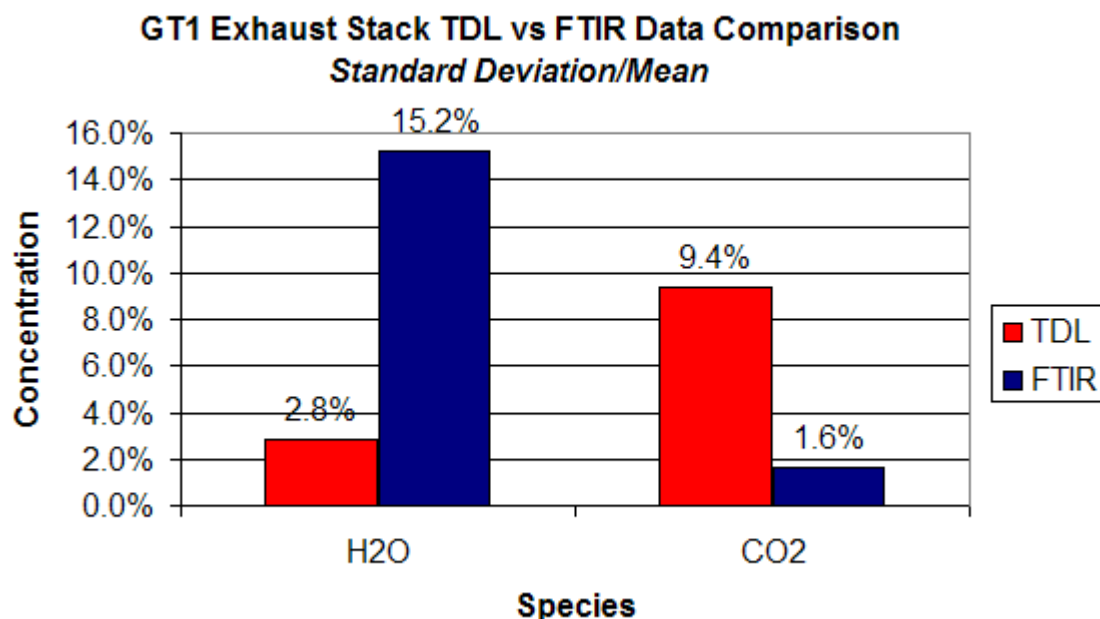
Figure 5.36: Ratio of the standard deviation to the mean for the TDL and FTIR GT1 exhaust stack data

Reviewing the TDL WMS H_2O and CO_2 line strength and pressure-broadening uncertainties are worthwhile. Much effort was taken during the laboratory calibration of the sensors to minimize these errors. Each data point in the line strength measurement represented 3 or 4 measurements with 20 samples each at a different pressure.

The maximum uncertainty in the TDL H_2O line strength measurement is approximately 11%, and most of the values are on the order of 3-4% (Gharavi 2004). These uncertainties take into account 1% error due to pressure measurement, 0.3% for

path length error, and 2% error for line strength function fitting. The primary uncertainty in the measured values of the line strengths is related to the background H_2O absorption in the region outside the static cell. These errors were minimized by the vacuum tube transition zones utilized in the glass and metal cell designs. In atmospheric combustion systems where the pressure broadening is on the order of Doppler broadening the overall uncertainty is on the order of 15% (Gharavi 2004). For the CO_2 experiments, the signal measurement errors across multiple spectra were about 1% or less of the measured concentration (Hartley 2006).

Another method for analyzing the TDL WMS error is to track the ratio of H_2O versus CO_2 concentration over the duration of the field-testing. This ratio is plotted against time in Figure 5.37.
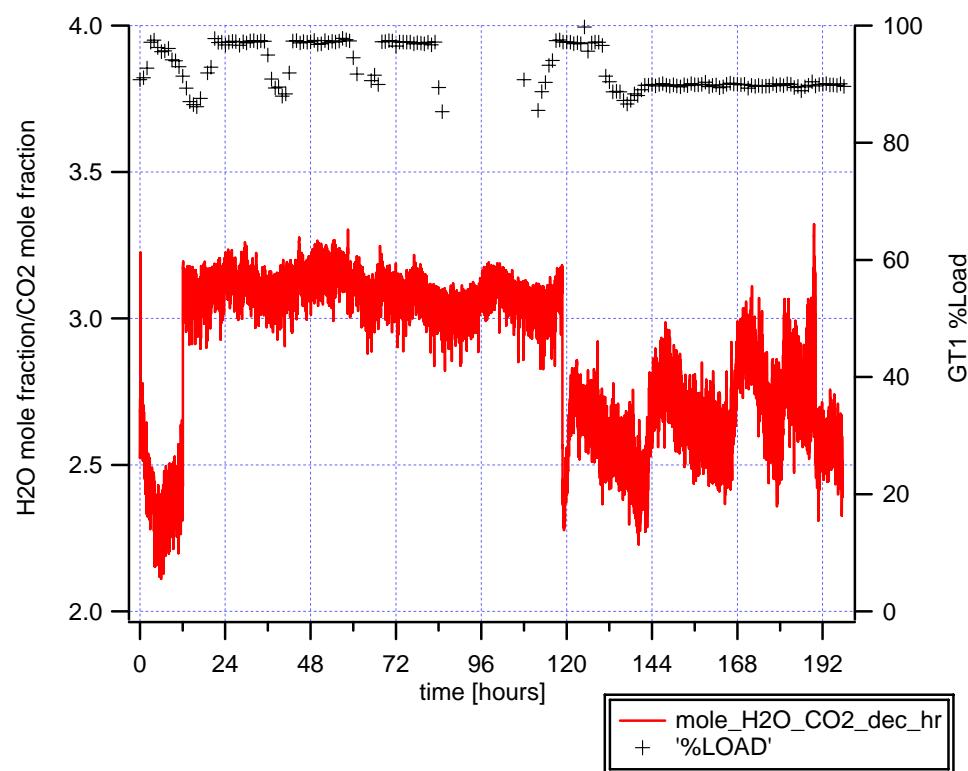
Figure 5.37: Ratio of H_2O and CO_2 mole fractions versus time along with GT1 percent load

Between hours 12 and 118, the CO2 signal was corrupted. Outside of this time period, the ratio was in the 2 to 3 range. The oscillation of the ratio does not appear to correspond to changes in turbine load, but rather may be indicative of something occurring within the instrument.

CHAPTER 6: Conclusion

Tunable Diode Laser Absorption Spectroscopy (TDLAS) provides an accurate, fast, and non-intrusive solution for species and temperature measurement. The application of this technology to measure temperature, H_2O, and CO_2 content from an industrial gas turbine has been demonstrated by this research. The multi-gas sensor system, consisting of inexpensive, commercially available, tunable diode lasers used in the telecommunications industry, uses Wavelength Modulation Spectroscopy (WMS) to quantify path-averaged temperature and concentrations.

H_2O and CO_2 spectroscopic information was first gathered in the laboratory and then the system was packaged for field use. The work culminated in an eight-day test in April 2006 where actual stationary gas turbine emissions data were captured. The results demonstrate the capability to measure temperature, H_2O, and CO_2 in an industrial environment using two tunable diode lasers. The results were compared against FTIR and Thermocouple (TC) data collected at the same site. The TDL WMS temperature measurements fell within the predicted accuracy of the sensor when compared with exhaust TC data. The TDL WMS H_2O concentration results exhibited fewer fluctuations and the CO_2 measurements exhibited higher fluctuations when compared to the commercially available FTIR analyzer. Large amounts of TDL WMS data were handled by filtering and decimating.

Future work could integrate the algorithms derived in this research to the Labview program to eliminate the need for post-processing the data. Another improvement would

be to add a TC input to the TDL WMS box so that TDL versus TC temperature comparisons could be made for the duration of the testing.

Future research should focus on real time measurement of NOx and CO along with temperature and CO_2. This data could be used for active control of gas turbines to optimize emissions performance. Quantum cascade laser technology is the most promising development for future species and temperature measurement of gas turbine exhaust, as there is a clear advantage to operating in the mid-infrared region. However, at this time quantum cascade lasers are still much more expensive than the telecommunication lasers used in this research.

Appendix

Bill of materials for the glass and metal cell assemblies:

M. Leon, UCSD TDL "Multiplexed Modulated Diode Laser System"
12/30/2006

	PURCHASED	CALC
	ALREADY IN LAB	ESTIMATE

FAB#: 3219
NRG5052

ITEM	PART	VENDOR	PN	QTY PER CELL	COST	# OF CELLS	TOTAL QTY	TOTAL COST
1	2" OD Fused Silica 1 Degree Wedge Window for Metal Cells	CVI Laser	LW-2-2037-UV	2	$195.00	2	4	$780.00
2	1" OD Fused Silica 1 Degree Wedge Window for Glass Cell	CVI Laser	LW-1-1037-UV	4	$105.00	2	12	$1,140.00
3	Glass cell, 30 cm long, for use with existing heater	Curtis Technologies		1	$390.00	2	2	$780.00
4	New H2O glass cell; 4 windows	Curtis Technologies		1	$650.00	1	1	$650.00
5	Glass Vacuum Tubes, 30 cm long, for use with metal cell configuration	Curtis Technologies		2	$310.00	1	2	$620.00
6	Ceramic Fiber Heater, 5" ID, Semi-Cylinder, 20" total L, 240V	Watlow		2	$800.00	1	2	$1,600.00
7	0.063" TC's, K Type, Closed Ended, 6 ft long, Ungrounded, Mini Male Connectors	Durosense	KSU-063-72inch-I-MP	6	$33.50	2	12	$402.00
8	MDC FLANGE, 2.73" OD, 6 hole	MDC	110014	5	$11.20	2	10	$112.00
9	MDC FLANGE, 1.33x0.5 Bore Flanges	MDC	110003	4	$9.60	2	8	$76.80
10	MDC 1.33" Gaskets	MDC		1	$13.30	2	2	$26.60
11	MDC FLANGE, 2.73" OD, 6 hole	MDC	110014	1	$11.20	2	2	$22.40
12	C-SEAL, External Pressure	Perkin-Elmer	633R9Y-0028-C	2	$78.41	1	12	$940.92
13	C-SEAL, Internal Pressure	Perkin-Elmer	613R9Y-0025-C	2	$78.41	1	12	$940.92
14	Conax Fittings, 0.062" Probe, 1/16" NPT, Graphoil Sealant (925 Deg. F)	CONAX	MPG-062-A-G	6	$27.00	2	12	$324.00
15	SS304 1.5" DIA. SEAMLESS TUBE, L=38.952", 0.049" Wall Thickness	McMaster-Carr	89895K783	1	$105.00	2	2	$210.00
16	1/4-28 Bolts, 1.75" long, 18-8 SST, Qty 50	McMaster-Carr	92198A112	12	$0.51	2	24	$12.18
17	1/4-28 Nuts, 18-8 SST, Qty 100	McMaster-Carr	91841A215	12	$0.29	2	24	$6.91
18	1/4" Washers, SST, Qty 100	McMaster-Carr	98017A660	24	$0.15	2	48	$7.08
19	1/4" Belleville Washers, SST	McMaster-Carr	9713K62	24	$0.35	2	48	$16.96
20	Silica insulation board for heater plugs and supports; 1" Thick; Max Temp 1925 Deg F	McMaster-Carr	6841K5	1	$159.83	1	1	$159.83
21	12" Dia Ducting to house heaters; 5' long	McMaster-Carr	1766K57	1	$22.92	1	1	$22.92
22	Mineral Wool Pipe Insulation to insulate heaters; 3' long	McMaster-Carr	9364K23	2	$23.33	1	2	$46.66
23	Band Clamps to hold heater support Structure together; 10 per pack	McMaster-Carr	45945K44	1	$8.22	1	1	$8.22
24	High Temp Refractory Cement; 2 quart	McMaster-Carr	9372K62	1	$8.63	1	1	$8.63
25	1/4" Elbow Weld On Fitting	Swagelok	SS-400-2-2W	3/1	$11.00	2	4	$44.00
26	1/4" Elbow Weld On Fitting	Swagelok	SS-400-2-4W	3/1	$11.00	2	4	$44.00
27	1/2" Elbow Weld On Fitting	Swagelok	SS-810-2-8W	2	$20.00	1	2	$40.00
28	1/2" to 1/4" Reducer	Swagelok	SS-400-R-8	2	$15.00	1	2	$30.00
29	1/4" Bellows Toggle Valve	Swagelok	SS-4BKT	2	$140.00	1	2	$280.00
30	1/4" Metering Needle Valve with Vernier	Swagelok	SS-SS4-VH	1	$80.00	1	1	$80.00
31	1/4" Metering Needle Valve	Swagelok	SS-SS4	1	$80.00	1	1	$80.00
32	1/4" Bellows Toggle Valve	Swagelok	SS-4BKT	4	$140.00	1	4	$560.00
33	1/4" Swagelok Tee	Swagelok	SS-400-3	10	$15.00	1	10	$150.00
34	1/4" Swagelok Port Connector	Swagelok	SS-401-PC	10	$3.00	1	10	$30.00
35	1.5" Tube by 1.5" Male NPT Swagelok Connector	Swagelok	SS-2400-1-24	1	$20.00	2	2	$40.00
36	Ceramic Fiber Heater, 5" ID, Semi-Cylinder, 20" total L, 240V	Watlow		4	$800.00	1	4	
37	DIN-A-MITE "A" Power Controller	Watlow	DA10-24CO-0000	3	$95.00	1	3	
38	Temperature Controller	Watlow	SD6C-HCAA-AARG	3	$153.00	1	3	
39	Graphoil sheet for non-sealing window/flange interface			1	$15.00	1	1	
40	1/4" Tubing for pressure and gas feeds			3	$0.00	2	6	
41	Mixer (V=2XMetalCellV)			1	$100.00	1	1	
							TOTAL	**$10,293.03**

References

Allendorf, S. W., Ottesen, D. K., Hardesty, D. R. Goldstein, D., Smith, C. W. and Malcomson, A. P. (1998). "Laser-Based Sensor for Real-Time Measurment of Offgas Composition and Temperature in BOF Steelmaking." <u>Iron and Steel Engineer</u> **74**: 31-35.

Arndt, R. (1965). "Analytical line shapes for Lorentzian signals broadened by modulation." <u>Journal of Applied Physics</u> **36**: 2522-2524.

Arroyo, M. P. and Hanson, R. K. (1993). "Absorption-Measurements of Water-Vapor Concentration, Temperature, and Line-Shape Parameters Using a Tunable Ingaasp Diode-Laser." <u>Applied Optics</u> **32**(30): 6104-6116.

Gharavi, M. (2004). "Infrared Optical Sensor for Combustion Diagnostics Using Wavelength Modulation Spectroscopy." <u>Mechanical Engineering</u>. College Park, MD, University of Maryland, College Park. Doctor of Philosophy.

Gharavi, M. and Buckley, S. G. (2004). "Single diode laser sensor for wide-range H_2O temperature measurements." <u>Applied Spectroscopy</u> **58**(4): 468-473.

Gharavi, M. and Buckley, S. G. (2005). "Diode laser absorption spectroscopy measurement of linestrengths and pressure broadening coefficients of the methane $2v_3$ band at elevated temperatures." <u>Journal of Molecular Spectroscopy</u> **229**: 78-88.

Hartley, C. (2006). "Infrared Laser Absorption Studies in a Combustion Exhaust Gas Simulator." <u>Mechanical Engineering</u>. La Jolla, CA, University of California San Diego. Master of Science.

Ku, R. T., Hinkley, E. D. and Sample, J. O. (1975). "Long-Path Monitoring of Atmospheric Carbon-Monoxide with a Tunable Diode Laser System." <u>Applied Optics</u> **14**(4): 854-861.

Liu, X., Jeffries, J. B., Hanson, R. K., Hinckley, K. M., and Woodmansee, M. A. (2006). "Development of a tunable diode laser sensor for measurements of gas turbine exhaust temperature." <u>Applied Physics B</u> **82**: 469-478.

Mann, Ch., Yang, K., Fuchs, F., Bronner, W., Kiefer, R., Koehler, K., Schneider, H., Kormann, R., Fischer, H., Gensty, T., and Elaesser, W. (2003). "Quantum Cascade Lasers for the Mid-infrared Spectral Range: Devices and Applications." Advances in Solid State Physics **43**: 351-368.

Mann, Ch. and Wagner, J. (2005). "Quantum Cascade Lasers: Valuable New Tools for Laser Spectroscopy." Photonics Spectra **39**(2): 74-80.

Mihalcea, R. M., Baer, D. S., Hanson, R. K. (1997). "Diode Laser Sensor for Measurements of CO, CO_2, and CH_4 in Combustion Flows." Applied Optics **36**(33): 8745-8752.

Mihalcea, R. M., D. S. Baer and R. K. Hanson (1998). Advanced Diode Laser Absorption Sensor for In-Situ Combustion Measurements of CO_2, H_2O, and Temperature. Proceedings of the Twenty-Seventh Symposium (International) on Combustion, Pittsburgh, PA.

Nagali, V., Chou, S. I., Baer, D. S., Hanson, R.K. and Segall, J. (1996). "Tunable Diode Laser Measurements of Methane at Elevated Temperatures." Applied Optics **35**(21): 4026-4032.

Nikkari, J. J., Di Iorio, J. M. and Thomson, M. J. (2002). "In Situ Combustion Measurement of CO, H_2O, and Temperature with a 1.58-mm Diode Laser and Two-Tone Frequency Modulation." Applied Optics **41**(3): 446-452.

Olivero, J. J. and R. L. Longbothum (1977). "Empirical Fits to Voigt Line-Width – Brief Review." Journal of Quantitative Spectroscopy & Radiative Transfer **17**(2): 233-236.

Philippe, L. C. and Hanson, R. K. (1993). "Laser Diode Wavelength Modulation Spectroscopy for Simultaneous Measurement of Temperature, Pressure, and Velocity in Shock-Heated Oxygen Flows." Applied Optics **32**: 6090-6103.

Reid, J. and D. Labrie (1981). "2nd-Harmonic Detection with Tunable Diode-Lasers - Comparison of Experiment and Theory." Applied Physics B-Photophysics and Laser Chemistry **26**(3): 203-210.

Rothman, L. S., D. Jacquemart, A. Barbe, D. C. Benner, M. Birk, L. R. Brown, M. R. Carleer, C. Chackerian, K. Chance, L. H. Coudert, V. Dana, V. M. Devi, J. M. Flaud, R. R. Gamache, A. Goldman, J. M. Hartmann, K. W. Jucks, A. G. Maki, J. Y. Mandin, S. T. Massie, J. Orphal, A. Perrin, C. P. Rinsland, M. A. H. Smith, J. Tennyson, R. N. Tolchenov, R. A. Toth, J. Vander Auwera, P. Varanasi and G. Wagner (2005). "The HITRAN 2004 molecular spectroscopic database." Journal of Quantitative Spectroscopy & Radiative Transfer **96**(2): 139-204.

Schilt, S. Thevenaz, L. and Phillipe, R. (2003). "Wavelength Modulation Spectroscopy: Combined Frequency and Intensity Laser Modulation." Applied Optics **42**(33): 6728-6738.

Schuger, A. (2006). "Diode Laser Measurment of H_2O, OH, and Temperature in a Premixed Methane and Air Flame through the Application of Wavelength Modulation Spectroscopy." Mechanical Engineering. La Jolla, CA, University of California, San Diego. Master of Science.

Stokes, L. F., Chodorow, M., and Shaw, H. J. (1982). "All-single-mode fiber resonator." Optical Society of America **7**(6): 288-290.

Teichert, H. Fernholz, T. and Ebert, V. (2003). "Simultaneous in situ Measurment of CO, H_2O, and Gas Temperatures in a Full-Sized Coal-Fired Power Plant by Near-Infrared Diode Lasers." Applied Optics **42**(12): 2043-2051.

Wahlquist, H. (1961). "Modulation broadening of unsaturated lorentzian lines." Journal of Chemical Physics **35**(5): 1708-1710.

Wehe, S., Allen, M., Lui, X., Jeffries, J., and Hanson, R.K. (2003). "NO and CO Absorption Measurements with a Mid-IR Quantum Cascade Laser for Engine Exhaust Applications." AIAA Paper No. 2003-0588, 41st AIAA Aerospace Sciences Meeting, Reno, NV.

Whiting, E. E. (1968). "An Empirical Approximation to Voigt Profile." Journal of Quantitative Spectroscopy & Radiative Transfer **8**(6): 1379-1384.

Wilson, G. V. H. (1963). "Modulation Broadening of NMR and ESR Line Shapes." Journal of Applied Physics **34**: 3276-3285.